INTERFACE

royalsocietypublishing.org/journal/rsif

Research

Cite this article: Lee S, Kwok N, Holsapple J, Heldt T, Bourouiba L. 2020 Enhanced wall shear stress prevents obstruction by astrocytes in ventricular catheters. *J. R. Soc. Interface* **17**: 20190884.
http://dx.doi.org/10.1098/rsif.2019.0884

Received: 24 December 2019
Accepted: 4 May 2020

Subject Category:
Life Sciences–Engineering interface

Subject Areas:
biomedical engineering

Keywords:
hydrocephalus, ventricular catheters, obstruction, astrocytes, wall shear stress, direct flow visualization

Author for correspondence:
L. Bourouiba
e-mail: lbouro@mit.edu

Electronic supplementary material is available online at https://doi.org/10.6084/m9.figshare.c.4979837.

THE ROYAL SOCIETY PUBLISHING

Enhanced wall shear stress prevents obstruction by astrocytes in ventricular catheters

S. Lee[1], N. Kwok[3], J. Holsapple[4], T. Heldt[2,3] and L. Bourouiba[1,2,3]

[1]The Fluid Dynamics of Disease Transmission Laboratory, and [2]Institute for Medical Engineering and Science, MIT, Cambridge, MA 02139, USA
[3]Health Sciences and Technology Program, Harvard Medical School, Boston, MA 02115, USA
[4]Department of Neurosurgery, Boston Medical Center, Boston, MA 02118, USA

TH, 0000-0002-2446-1499; LB, 0000-0001-6025-457X

The treatment of hydrocephalus often involves the placement of a shunt catheter into the cerebrospinal ventricular space, though such ventricular catheters often fail by tissue obstruction. While diverse cell types contribute to the obstruction, astrocytes are believed to contribute to late catheter failure that can occur months after shunt insertion. Using *in vitro* microfluidic cultures of astrocytes, we show that applied fluid shear stress leads to a decrease of cell confluency and the loss of their typical stellate cell morphology. Furthermore, we show that astrocytes exposed to moderate shear stress for an extended period of time are detached more easily upon suddenly imposed high fluid shear stress. In light of these findings and examining the range of values of wall shear stress in a typical ventricular catheter through computational fluid dynamics (CFD) simulation, we find that the typical geometry of ventricular catheters has low wall shear stress zones that can favour the growth and adhesion of astrocytes, thus promoting obstruction. Using high-precision direct flow visualization and CFD simulations, we discover that the catheter flow can be formulated as a network of Poiseuille flows. Based on this observation, we leverage a Poiseuille network model to optimize ventricular catheter design such that the distribution of wall shear stress is above a critical threshold to minimize astrocyte adhesion and growth. Using this approach, we also suggest a novel design principle that not only optimizes the wall shear stress distribution but also eliminates a stagnation zone with low wall shear stress, which is common to current ventricular catheters.

1. Introduction

Hydrocephalus is a disease of the cerebrospinal fluid (CSF) circulation that often manifests with enlarged cerebral ventricles due to excess CSF in the cerebral ventricular system [1]. The shunt (figure 1*a*), a catheter-based CSF drainage system, has been widely employed to treat this condition. A typical shunt is made of a proximal (ventricular) catheter (figure 1*b*), a shunt valve and a distal catheter. The ventricular catheter is placed in the cerebral ventricles, and the distal catheter is placed elsewhere in the body for drainage. When the ventricular CSF pressure, also known as intracranial pressure (ICP), rises and the pressure differential across the valve becomes larger than a prescribed threshold, the valve opens and drains CSF from the ventricles, most often into the abdominal cavity or the right atrium [2].

In pediatric patients, the shunt system has a low lifespan, particularly due to obstruction occurring at the ventricular catheter by brain tissue [3]. A recent prospective study reported that 60% of pediatric shunts fail within 2 years, and the obstruction of the ventricular catheter is the most frequent cause, accounting for 27% of such failures [4]. Obstruction causes acute symptoms to patients, such as headaches, nausea, vomiting, irritability, cranial nerve palsies, blindness and

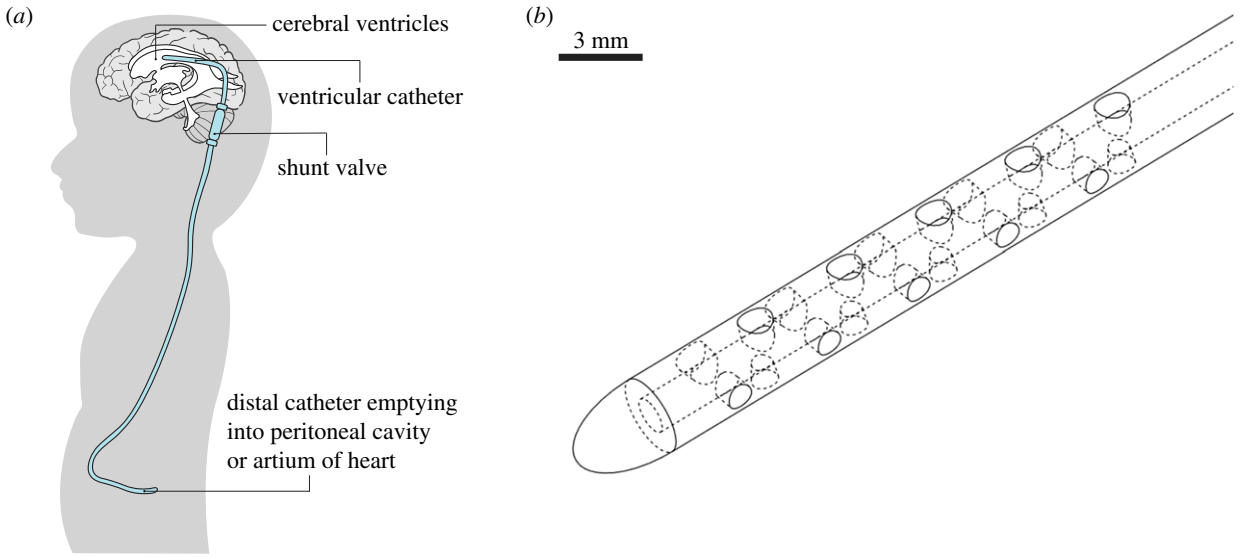

Figure 1. (*a*) Illustration of shunt system. (*b*) Example of three-dimensional model of ventricular catheter, reconstructed from measurement of a Codman EDS 3 Clear Ventricular CSF Catheter [16].

even death. Thus, shunt obstructions require urgent shunt revision surgery, which carries the risk of infection and damage to brain tissue [5–8]. Although there is a variety of ventricular catheter designs commercially available, none have been shown in clinical trials to be superior in preventing obstruction [8].

Recent studies based on immunostaining of explanted ventricular catheters found that glial tissue ingrowth, mainly by astrocytes and microglia, is the most frequent culprit of obstructions [9,10]. Astrocytes and microglia are involved in the immune response of the central nervous system, forming dense glial tissue around foreign bodies such as neural electrodes [11] and ventricular catheters [9,10]. It has been reported that microglia first migrate to the catheter after shunt insertion and astrocytes gradually become the dominant cell type forming fibrous tissue in the catheter [9,10]. Given that astrocyte-dominant tissue typically becomes prevalent on the catheter surface in the late stage of cellular response to a catheter (greater than two months) [10], improving the shunt lifespan by years necessitates hindering astrocytic tissue formation.

Astrocytes on the inner walls of an implanted ventricular catheter encounter CSF flow (figure 2). This CSF flow touching the inner walls induces a shear stress to the walls (i.e. wall shear stress). As the size of astrocytes (approx. 10 µm) is much smaller than the characteristic length scale of a ventricular catheter hole (approx. 500 µm), we can assume that the fluid shear stress imposed by the CSF on the astrocytes is given by the wall shear stress. Since astrocytes are exposed to the shear stress imposed by the CSF flow and given the significant finding of astrocyte aggregation in shunt catheters, this study focuses on understanding astrocyte behaviour in response to fluid shear stress, which is one possible fluid-dynamic design parameter to help suppress astrocytic tissue formation.

The behaviour of astrocytes under long-term fluid shear stress is poorly understood, particularly in the context of ventricular catheter obstruction. Cornelison *et al.* [12] reported that when cocultured astrocytes and microglia are exposed to *in vitro* fluid shear stress for 1 h, they exhibit increased S1P3 expression which is upregulated in pro-inflammatory conditions [13]. Given that astrocytes in the inflammatory state can proliferate [14], the implication from this study is

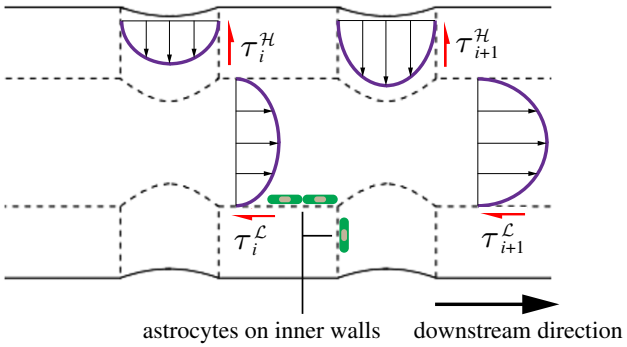

Figure 2. Wall shear stress, τ_i, formed at the inner surfaces of holes and lumina due to CSF flow. The wall shear stress is assumed to be the fluid shear stress imposed on the astrocytes (shown in green) coating the walls. Holes that face each other have the same wall shear stress due to geometric symmetry. The subscript denotes the index of a segment that is counted from the catheter tip. The superscripts $\mathcal{H}$ and $\mathcal{L}$ represent hole and lumen, respectively. Wall shear stress defined here is the spatially averaged value.

that fluid shear stress may enhance astrocyte proliferation. However, experimental results from Harris *et al.* [15] suggest that astrocytes are vulnerable to fluid shear stress particularly on longer timescales (approx. 10 h). The authors performed bioreactor studies in which astrocytes were allowed to migrate from an artificial brain parenchyma tissue mimic surrounding a ventricular catheter. They found that a flow culture of 18 h perfusion resulted in a lower number of astrocytes on ventricular catheters when compared with a static culture. We hypothesize that the lower number of astrocytes in the flow culture is either due to forced cell detachment by the shear stress or hindered cell proliferation.

To explore this hypothesis and to understand the behaviour of astrocytes under long-term fluid shear stress, we performed *in vitro* microfluidic experiments that imposed fluid shear stress on astrocytes for 48 h. We find that the long-term fluid shear decreases astrocyte confluency, which is the area percentage covered by cells and is an estimate of cellular growth rate. Additionally, we find a loss of the stellate cellular morphology, typical of healthy astrocytes (§2.2). Instead, the cells appear to form aggregates. Moreover, we find that astrocytes exposed to

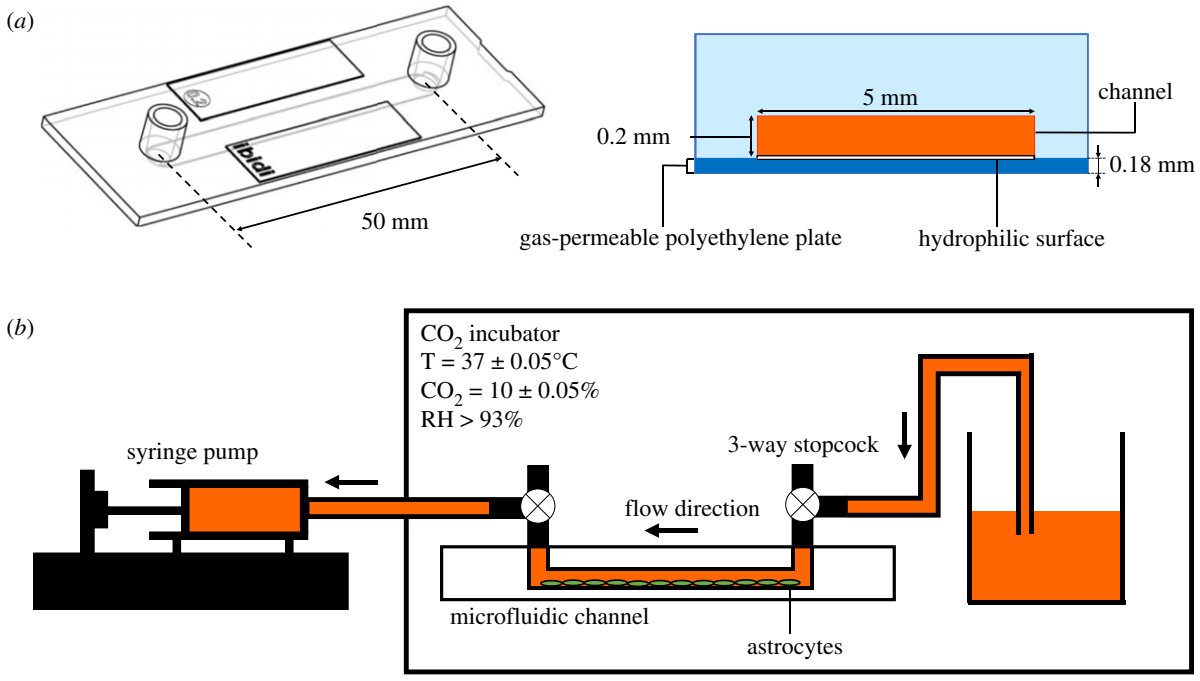

Figure 3. (*a*) Transparent microfluidic channel used in this study (left) [18] and illustration of channel cross-section (right), with a bottom plate that is gas-permeable so that pH remains controlled with sufficient gas exchange. The bottom surface is chemically treated for adherence of cells. (*b*) Schematic of microfluidic experiment set-up embedded in controlled CO_2 environmental chamber.

long-term fluid shear are detached more easily upon sudden transition to high fluid shear stress (§2.3). In light of the findings that astrocytes are vulnerable to long-term fluid shear stress, we show that the typical geometry of current ventricular catheters may promote astrocyte obstruction due to the inherent presence of regions with comparatively low wall shear stress. Using computational fluid dynamic (CFD) simulations of the flow in a typical ventricular catheter, and using a Poiseuille network model (PNM) proposed in this study, we conducted dimensional analyses of a typical ventricular catheter and derived a general design principle to optimize the wall shear stress distribution (§4). We also identify and discuss another weak point of typical ventricular catheters, which is the formation of a stagnation zone with low wall shear stress. Finally, we propose a novel ventricular catheter geometric design principle that both optimizes the wall shear stress distribution and eliminates the stagnation zone (§4.5).

2. Astrocytes vulnerable to long-term fluid shear stress

2.1. Microfluidic experiment set-up

We cultured a mouse astrocyte cell line (C8D1A, ATCC) in a commercial transparent microfluidic channel (μ-Slide I Luer, ibidi GmbH) to investigate the response of astrocytes under fluid shear stress (figure 3). Two cases were studied with the channel: (1) a static culture with zero fluid shear stress and (2) a flow culture with fluid shear stress of 3 mPa. The culture medium was Dulbecco's Modified Eagle's Medium (D6429, Sigma), supplemented with 10% fetal bovine serum (FBS001, Neuromics), 1% penicillin–streptomycin (#15140122, Gibco) and 2.5 U ml^{-1} nystatin (N6261, Sigma). Using a high-precision rotational rheometer (HR-1, TA Instruments), the viscosity of the medium was measured to be 1 mPa s at 37°C. Both cultures were maintained at 37°C in a humidified atmosphere of 10% CO_2. Astrocytes were first cultured in flasks until their confluency reached 80–90% and then seeded into the channel with a seeding density of 2.0×10^4 cells cm^{-2}. Seeded astrocytes were pre-cultured for 24 h in the channel to ensure cell adhesion. In this study, $T = 0$ h is defined as the time immediately after preculture. Passage numbers 8–11 upon delivery from ATCC were used in all experiments, where the passage number refers to the number of times a cell culture was subcultured.

For the static culture, the medium was changed every 24 h to ensure sufficient nutrient supply. For mammalian cell cultures in flasks, it is usually recommended to use a medium supply rate of 0.07–1 ml cm^{-2} d^{-1} [17]. In our case, the medium supply rate was 0.09 ml cm^{-2} d^{-1}, within the recommended range. We also confirmed that a medium supply rate of 0.18 ml cm^{-2} d^{-1} did not result in a statistical difference in confluency evolution. For the flow culture, as illustrated in figure 3*b*, the equilibrated medium with pH 7.4 was injected into the microfluidic channel by a syringe pump with constant flow rate of 6 µl min^{-1} to achieve 3 mPa of uniform wall shear stress across the channel's bottom surface. This wall shear stress was less than one-tenth of the wall shear stress that induced instant forced detachment of the cells. We monitored the pH of both cultures using pH strips and observed that a pH of 7.1–7.4 was maintained in both cultures. The cultures were maintained until $T = 48$ h. Phase-contrast microscopy (Ti-U, Nikon) was performed every 24 h to monitor changes in cell confluency and morphology.

2.2. Decrease of confluency and change in cell morphology upon long-term fluid shear stress

Astrocytes in static culture exhibited a gradual increase of confluency and maintained their star-shaped/stellate morphology that is the typical shape of physiological astrocytes; this stellate shape is commonly observed in both nonreactive and reactive astrocytes [19]. By contrast, astrocytes under prolonged fluid

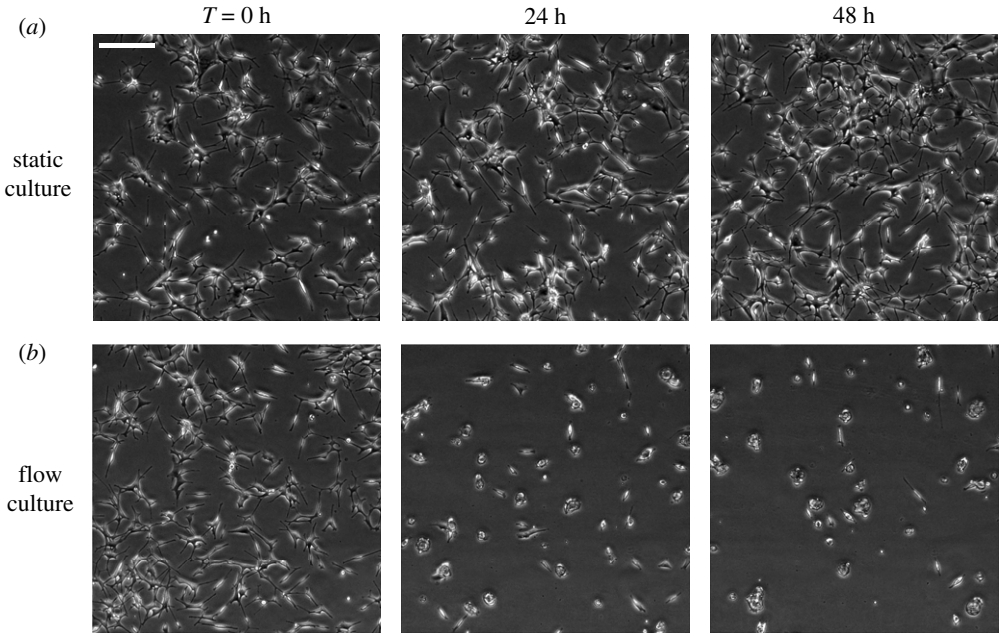

Figure 4. Phase-contrast imaging of static (*a*) and flow (*b*) cultures, showing clear difference in confluency of cells over time (up to 48 h here). Scale bar is 200 µm.

shear stress showed a decrease in confluency within the first 24 h, a loss of their characteristic star-like morphology, and the formation of cell aggregates (figures 4 and 5). Confluency was estimated across a region where fluid shear stress was homogeneous (electronic supplementary material, S3) and measured using a segmentation method proposed by Jaccard *et al.* [20] (electronic supplementary material, S4). The loss of characteristic projections under applied fluid shear stress may suggest cytotoxicity of long-term fluid shear stress to astrocytes as such loss is frequently observed in astrocytes with pathological conditions [21–24]. Also, cellular aggregates found on explanted ventricular catheters showed an extensive mesh of astrocytes with characteristic cellular projections emanating from the cell bodies [10], characteristic of healthy astrocytes, which we found in our static cell culture but not in the flow culture.

2.3. Long-term fluid shear stress facilitates forced detachment by high fluid shear stress

We further observed that astrocytes exposed to long-term moderate fluid shear stress were more easily detached from the surface upon sudden imposition of high fluid shear stress. At $T = 72$ h, both static and flow cultures were subjected to a sudden high fluid shear stress of 30 mPa. Here, the ramping time from 0 to 100% of flow rate was about 17 ± 3 s (SD with $n = 3$), indeed a much shorter ramping time than the 163 ± 24 s (SD with $n = 3$) used for imposition of continuous flow rate conditions in other experiments. The channels were exposed to the high fluid shear stress for 1 min and were imaged via phase-contrast microscopy to subsequently digitally quantify the resultant change in confluency. We performed this procedure three times for each channel, with a 3-min total exposure time to high shear stress. This high fluid shear stress corresponds to a level that can be found in typical ventricular catheters with flow rates of $Q = 1$ ml min^{-1}, a reported upper bound on shunt flow rate [25,26]. We observed that after 3 min, astrocytes cultured under continuous moderate shear stress showed a 44 ± 14% decrease in relative confluency (defined as confluency normalized by the initial confluency) due to both detachment and cell retraction. In contrast, static

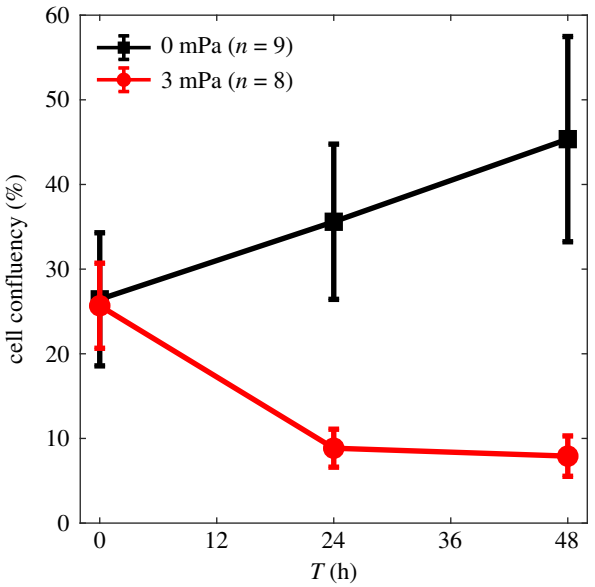

Figure 5. Quantification of change of cell confluency over time in static (0 mPa shear stress) and flow (3 mPa shear stress) cultures, such as those shown in figure 4. Error bars reflect the standard deviation over *n* number of independent experiments performed.

cultured astrocytes exhibited a 22 ± 6% decrease, but *solely* due to cell retraction (figures 6 and 7). The videos provided in electronic supplementary material, movie S1, show that the detachment upon high shear stress only occurs to astrocytes cultured under continuous moderate shear stress, in contrast to astrocytes statically cultured, which appear more robustly attached and instead only show a change in morphology in response to the suddenly imposed high shear stress condition.

Although little information is available on the temporal change of shunt flow rates, we can expect that the flow rate fluctuates with changes in ICP, which can be caused by posture change or respiratory variation in ICP that cause intermittent opening of the shunt valve [25,27]. According to a bench test with actual catheters, with mathematical models of ICP, the flow rate can attain maximum values close to 1 ml min^{-1} [25]. We performed a CFD simulation with 1 ml min^{-1} of the flow

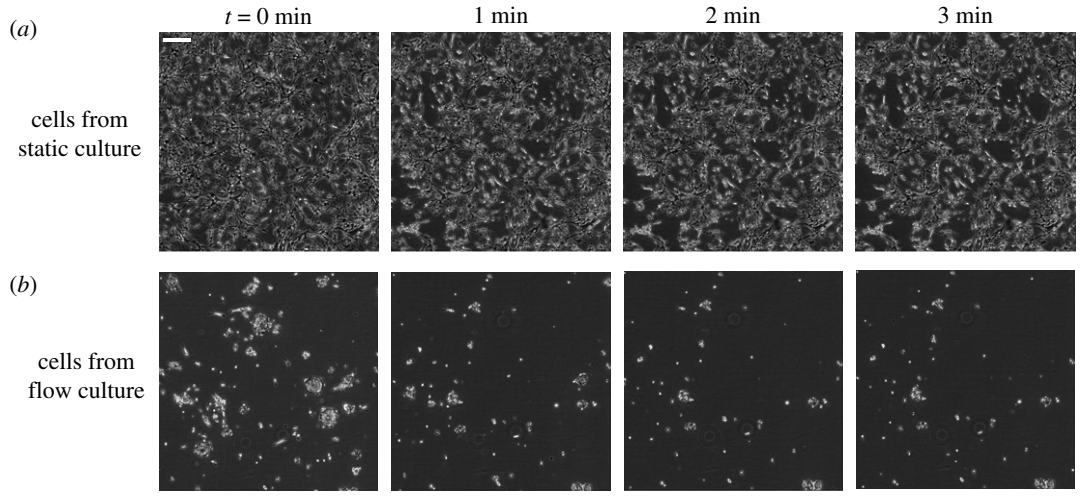

Figure 6. Phase contrast imaging of the response of astrocytes to short high fluid shear stress of 30 mPa at $T = 72$ h. Here (above each column), t is the duration for which the high fluid shear stress is imposed. Astrocytes cultured under continuous long-term moderate fluid shear stress (*b*) exhibit more detachment, while those from static culture (*a*) only show change in cell morphology, with noticeable regions of cell retraction. Scale bar is 200 µm. The videos are provided in electronic supplementary material, movie S1.

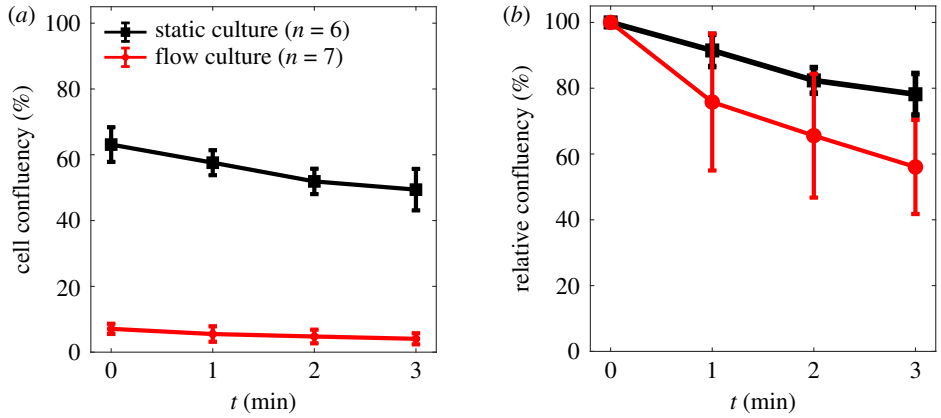

Figure 7. (*a*) Changes of confluency of astrocytes from the static and flow cultures when subjected to 30 mPa fluid shear stress computed from images such as those shown in figure 6. (*b*) Changes of relative confluency corresponding to (*a*), normalized by confluency value at $t = 0$ min. The difference in relative confluency between the static and flow cultures increases over time. At $t = 3$ min, the difference between the groups is 22%, a statistically significant difference ($p < 0.05$ of a two-sided Mann–Whitney U test). Error bars give the standard deviation across independent experiments (n).

rate in the catheter given in figure 1*b* and observed that the wall shear stress at the most downstream lumen was larger than 50 mPa. This implies that astrocytes in an actual ventricular catheter can be exposed to fluid shear stress that induces forced detachment—as shown in our experiment—and which can be enhanced by long-term fluid shear stress whose fluctuating timescale and amplitude in patients were observed to be of the order of $O(1\text{ h})$ and $O(0.1\text{ ml min}^{-1})$, respectively [28].

Ultimately, the experimental results shown in this section provide a key insight for a new approach to the design of ventricular catheters: *How can wall shear stress distribution on the inner wall surfaces be optimized to hinder obstructive astrocytic glial tissue formation?*

3. Formation of low wall shear stress zone in typical ventricular catheter

3.1. Computational fluid dynamics simulation set-up

In the light of our discovery of the vulnerability of astrocytes to long-term fluid shear stress, we performed CFD simulations (Fluent 2019 R1) to investigate the wall shear stress distribution in typical ventricular catheters. In this study, we considered a case where the cerebral ventricles are so enlarged that frictional loss from the ventricular wall is negligible. We ensured this condition in the simulation by enclosing the ventricular catheter into a box domain whose walls are sufficiently distant from the catheter (figure 8), which also meets the distance condition suggested by Weisenberg *et al.* [29]. We imposed a constant normal velocity condition on the surface of the domain that faces the tip of the catheter and zero-pressure condition on the outlet of the catheter. A no-slip boundary condition is applied to the other walls.

Flows in ventricular catheter have low Reynolds numbers (Re); thus, a laminar model that solves the incompressible Navier–Stokes equations was used in all simulations. Re is defined as

$$Re = \frac{\rho U D}{\mu}, \tag{3.1}$$

where U is the mean velocity at the outlet of the catheter, D is the lumen diameter, ρ and μ are the density and viscosity of CSF, respectively. The density of CSF is $\approx 1000\text{ kg m}^{-3}$ [30].

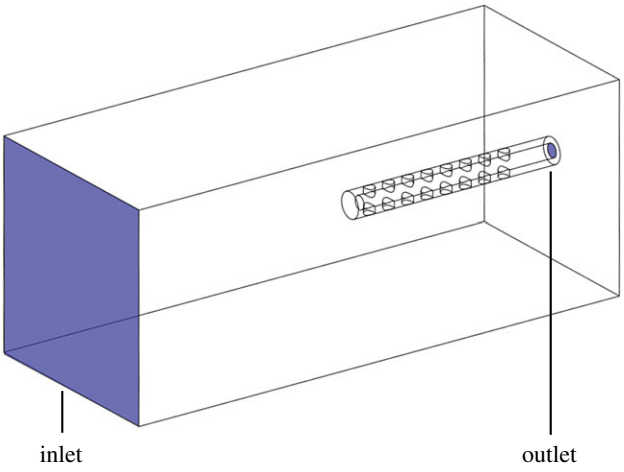

Figure 8. Example of three-dimensional models used in our CFD simulations. The size of the domain is set to be sufficiently large, to ensure negligible wall effects, including frictional loss. The inlet and outlet have constant-velocity and zero-pressure conditions, respectively. No-slip boundary conditions are imposed on the other walls.

We measured the viscosity of CSF from human subjects, finding that its viscosity ranges from 0.8 to 1.8 mPa s with weak shear thinning (see electronic supplementary material, S6 for details). This result differs from a prior report that CSF is Newtonian [31]. The prior study had insufficient measurements of viscosity with shear rates below 360 s^{-1}, across which shear thinning starts to become noticeable according to our data. D is within 1.0–1.6 mm [2], and an upper bound of the shunt flow rate was reported to be $\simeq$1 ml min^{-1} [28]. Given these values, the physiological Re is estimated to be less than 25, mostly a laminar flow. Based on the values from the literature and our measurement, ρ and μ were set to be 1000 kg m^{-3} and 0.8 mPa s, respectively, in all our simulations.

3.2. Quasi-exponential decay of wall shear stress across typical ventricular catheters

Figure 9 shows the design of a typical ventricular catheter. Here, a typical ventricular catheter represents a catheter whose holes have the same diameter, depth, spacing interval, and number of holes per segment. From CFD simulations, we found that the typical ventricular catheter features a quasi-exponential decay of MWSS over decreasing index of holes or lumina (figure 10). This exponential decay leaves many holes with low WSS, which can be favourable to the adhesion and growth of astrocytes. In the simulation, we set the flow rate Q to 0.03 ml min^{-1} which is 10% of the typical CSF production rate in the cerebral ventricular system [32]. This flow rate represents a physiological lower bound of the shunt flow rate, which we consider to be a worst-case scenario in terms low WSS values insufficient to alter astrocyte dynamics and adhesion.

We observed from the astrocyte experiments (§2) that fluid shear stress of approximately O(1 mPa) prevents astrocytes from increasing confluency and from maintaining their healthy morphology. When applying 1 mPa as a cut-off WSS to the simulation in figure 10, we conclude that all holes and lumina except H8 and L8 have WSS that are lower than the ideal threshold condition that could prevent obstruction. This implies that a typical ventricular catheter may not have sufficient WSS across all inner surfaces if it is designed without particular consideration for the optimization of WSS distribution. We thus turn towards a more systematic approach to optimize the ventricular catheter design to ensure WSS values hindering astrocyte attachment and potential for obstruction.

4. Optimization of typical ventricular catheter using dimensional analysis

4.1. Poiseuille flow in ventricular catheters

Building on the key combined insights that (1) astrocytes are vulnerable to fluid shear stress and (2) they can play a major role in catheter obstruction, maximizing the WSS inside a ventricular catheter is a valuable strategy to reduce obstruction. This requires understanding the characteristics of the flow within typical catheters. To develop this understanding, we performed direct flow visualization on an actual catheter (Codman EDS 3 Clear Ventricular Catheter, Codman & Shurtleff), using direct fluorescent particle tracking performed by high-speed fluorescent microscopy (Ti-U, Nikon). Given the curvature of catheter tubing, accurate measurements required optical correction of the curvature-induced image distortions. We did this with refractive index matching between the chosen working liquid and the material of the catheter. The details of the experimental methodology, including the calculation enabling us to determine the optimal choice of refractive index matching are in Lee [33] and Saksena *et al.* [34].

From the visualization experiments, we first found that the flow entering a hole does not have a uniform velocity profile (figure 11*b*). The entrance length l at which a laminar flow becomes fully developed classically follows $l/d = 0.06Re$, where d is the hole diameter [35]. Assuming that the flow enters a catheter hole with a uniform velocity profile, the entrance length l would be $\sim O(0.1d)$ for a hole with local Reynolds number $Re \sim O(1)$. In fact, our measurements (e.g. electronic supplementary material, movie S2) show that the flow profile is pre-developed from the outside of the hole, inducing an entrance length that is shorter than that expected from classical estimates. Indeed, Sparrow & Anderson [36] performed numerical simulations of a two-dimensional flow that is drawn from a large reservoir to a channel, finding that the entrance length for $Re = 25$—which is the highest Re in a catheter system—to be around 35% of the channel height. Note that the classical entrance length estimation gives 150% of the height [35], four times larger than the value for a flow from the large reservoir to a small channel. This implies that the flow at the catheter hole would become a fully developed Poiseuille flow shortly upon hole entrance. Given the lack of prior quantitative flow measurements in such catheter systems [37], we had to directly measure the actual velocity profiles at the catheter holes to confirm the nature of the flow profiles.

Figure 12*a*,*b* shows an example of direct experimental measurements of velocity profile at a catheter hole. First, this measured—reconstructed from particle tracking—profile matches well the associated flow rate-matched theoretical fully developed Poiseulle flow profile, with a 5% error, showing excellent agreement with the Poiseuille fully developed flow hypothesis (figure 12*c*). In this comparison, the flow rate was computed from integration of the experimentally measured flow profile. Second, we also compare the CFD predicted flow profile against the measured profile—again, reconstructed from particle tracking—and find 12% error, showing that the

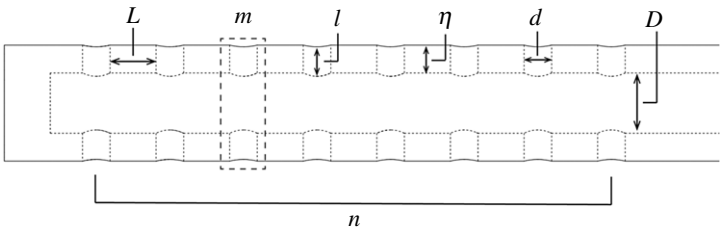

Figure 9. Schematic of a typical ventricular catheter and its geometric parameters. Every hole has the same diameter d, depth l, wall thickness η, and spacing interval L. Each hole segment (dashed box) has m holes, and the total number of hole segments is n.

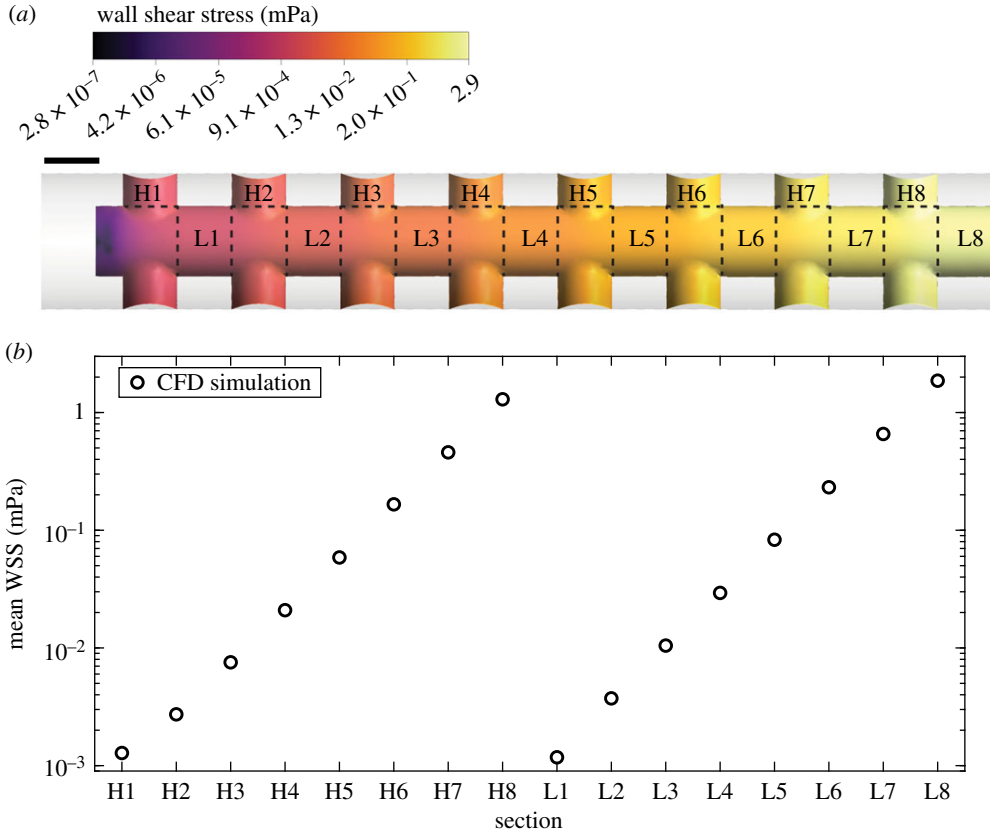

Figure 10. Results of CFD simulations discussed in §3.2 on a typical ventricular catheter with total flow rate of 0.03 ml min^{-1}, which is 10% of a typical CSF production rate. (*a*) Wall shear stress contour inside the catheter. Scale bar is 1 mm. (*b*) Spatially averaged mean wall shear stress at each catheter section shown in schematic (*a*).

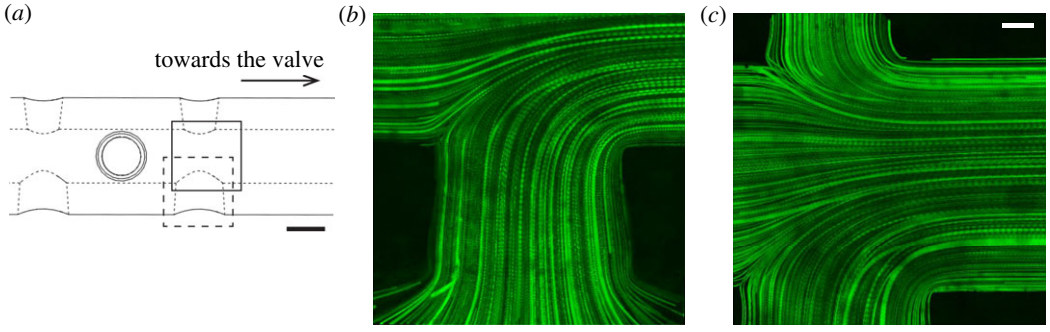

Figure 11. Flow visualization at a hole closest to the valve, using fluorescent particle tracking by high-speed microscopy. (*a*) Dashed and solid boxes indicate the region of interest in (*b*) and (*c*), respectively. Scale bar is 1 mm. (*b*,*c*) Pathlines of fluorescent particles illustrate the entry of a flow, followed by the confluence of flows in the lumen. In both (*b*,*c*), the Reynolds number, (3.1), is 0.5. The plane of focus of the microscope objective was located to the middle plane of the catheter. Scale bar in (*c*) is 200 µm and also applies to (*b*). The videos of (*b*) and (*c*) are given in electronic supplementary material, movie S2.

CFD prediction is also reasonable (figure 12*d*). Here, the error is defined as $\|\mathbf{V}-\mathbf{V}_{\mathrm{exp}}\|_2/\|\mathbf{V}_{\mathrm{exp}}\|_2$, where $\mathbf{V}$ is a vector, the predicted velocity at all grid nodes, and $\mathbf{V}_{\mathrm{exp}}$ is the corresponding vector from the experimentally measured velocity profile. The step size of the grid is 1% of the diameter of the cross-section.

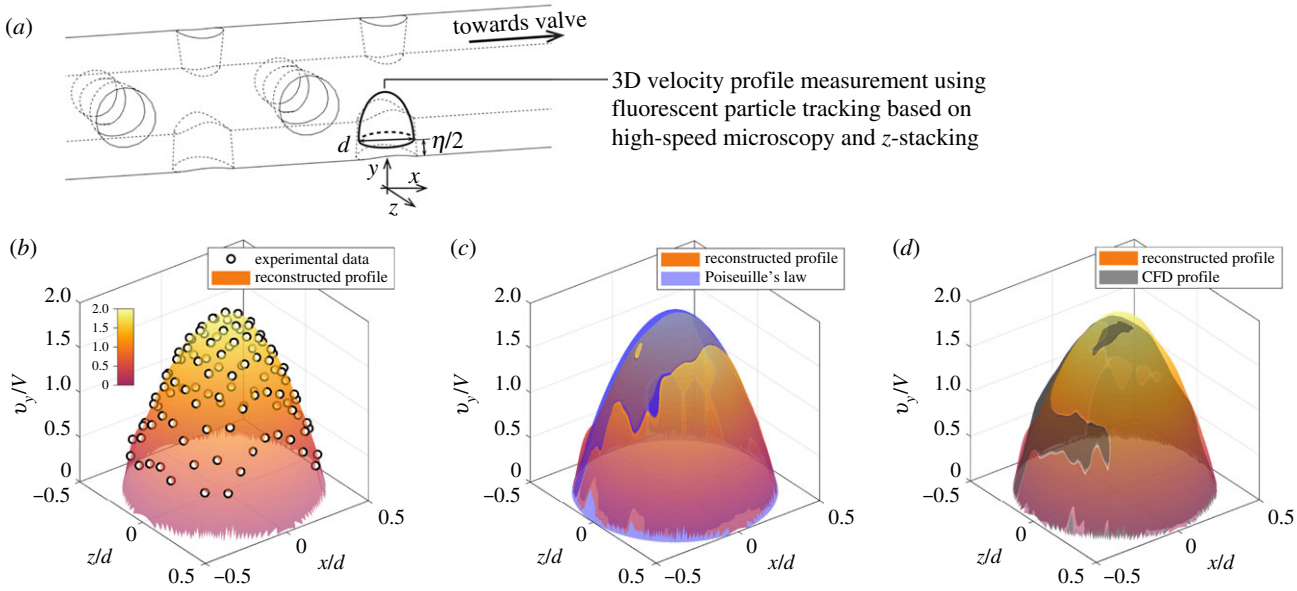

Figure 12. Measurement of three-dimensional velocity profile. (*a*) Velocity profile at a catheter hole closest to the valve was measured by direct particle tracking with high-speed imaging coupled to fluorescent microscopy. Using vertical layering of images, or *z*-stacking, we directly measured the three-dimensional velocity profile at the middle plane of holes. (*b*) Directly measured velocity profiles. Two-dimensional velocity profiles at different *z*-locations are given in electronic supplementary material, S1 with more details including error bars. (*c*) Poiseuille flow profile matches very well the measured profile. (*d*) The profile calculated by CFD analysis shows also a reasonable agreement with the directly measured profiles. Here, the Reynolds number, (3.1), is 1, and *d* and *V* are the diameter of the cross-sectional area and the mean *y*-directional velocity over the area, respectively.

Additionally, we also performed CFD simulations for a flow with higher inertia ($Re = 25$) confirming that the flows in holes and the lumen remain well approximated by a Poiseuille profile (electronic supplementary material, S1).

4.2. Poiseuille network model and identification of dimensionless numbers

Having validated that the flow is indeed of Poiseuille type in most of the relevant regions of a typical catheter (figure 12), we discuss here a PNM we developed to describe a typical ventricular catheter as a multi-pipe system where Poiseuille flow applies at every section. From the model, we identified dimensionless numbers that determine the wall shear stress distribution inside a catheter. Using CFD simulations, we validated this approach, showing that the matched dimensionless numbers across different structural models lead to the same wall shear stress distribution as that of the PNM developed and discussed in detail in electronic supplementary material, S2.

The PNM consists of the following. Consider a typical ventricular catheter with lumen diameter D, hole diameter d and depth l, hole spacing interval L, wall thickness η, m number of holes per segment and n number of segments (figure 9). Here, we assume that the hole depth, l, is approximately the wall thickness η. Using the PNM, we predict the spatially averaged MWSS at the inner surface of a hole or lumen as

$$\sum_{i=1}^{k} \hat{\tau}_i^{\mathcal{H}} = \frac{l/L}{m(d/D)^4}(\hat{\tau}_{k+1}^{\mathcal{H}} - \hat{\tau}_k^{\mathcal{H}}) \quad \text{for } 1 \le k \le n-1, \tag{4.1}$$

$$\sum_{i=1}^{n} \hat{\tau}_i^{\mathcal{H}} = \frac{1}{m(d/D)^3} \tag{4.2}$$

and

$$\hat{\tau}_k^{\mathcal{L}} = m\left(\frac{d}{D}\right)^3 \sum_{i=1}^{k} \hat{\tau}_i^{\mathcal{H}} \quad \text{for } 1 \le k \le n, \tag{4.3}$$

where $\hat{\tau}_k^{\mathcal{H}}$ and $\hat{\tau}_k^{\mathcal{L}}$ are the MWSS values at the kth hole and lumen, respectively, both non-dimensionalized by the most downstream wall shear stress $\tau_d = 32\mu Q/\pi D^3$. Here, the subscript index is counted from the tip of the catheter. Equations (4.1) and (4.2) complete a system of linear equations that estimates the MWSS levels across holes, which in turn allows equation (4.3) to calculate the MWSS levels across lumina. Solving equation (4.1) allows us to express every $\hat{\tau}_k^{\mathcal{H}}$ as a function of $\hat{\tau}_1^{\mathcal{H}}$:

$$\hat{\tau}_k^{\mathcal{H}} = \left(\frac{\alpha^k + \alpha^{1-k}}{\alpha + 1}\right)\hat{\tau}_1^{\mathcal{H}} = G_k \hat{\tau}_1^{\mathcal{H}}, \tag{4.4}$$

where

$$\alpha = 1 + \frac{c + \sqrt{c^2 + 4c}}{2} \quad \text{and} \quad c = \frac{m(d/D)^4}{l/L}. \tag{4.5}$$

Detailed steps for solving the recursive relation (4.1) are given in electronic supplementary material, S2.

From (4.1) to (4.3), four dimensionless numbers associated with a typical ventricular catheter can be identified

$$m, \quad n, \quad \hat{l} = l/L \quad \text{and} \quad \hat{d} = d/D. \tag{4.6}$$

Using CFD simulations, we confirmed that catheter flows that have the same set of the dimensionless numbers share the same non-dimensionalized MWSS distribution (figure 13). Moreover, the non-dimensional MWSS distribution calculated from the PNM showed an excellent agreement with those obtained from the CFD simulations, themselves confirmed by direct flow reconstruction from microscopy particle tracking (figure 12). We studied three different scenarios to show that the PNM offers a universal principle for the description of the flow inside a typical ventricular catheter. While maintaining $m = 2$, $n = 8$, $\hat{l} = 0.6$ and $\hat{d} = 0.77$, the three different scenarios were designed to have different dimensional parameters and Reynolds numbers as given in figure 14 and

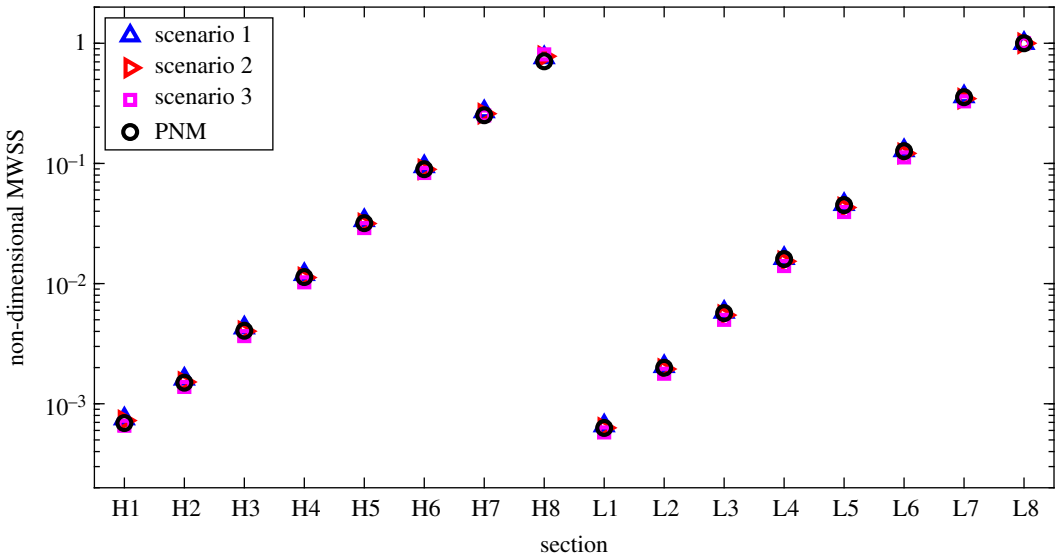

Figure 13. Non-dimensional MWSS distributions in three different scenarios, obtained from CFD simulations. All scenarios share the same $m = 2$, $n = 8$, $\hat{l} = 0.6$ and $\hat{d} = 0.77$.

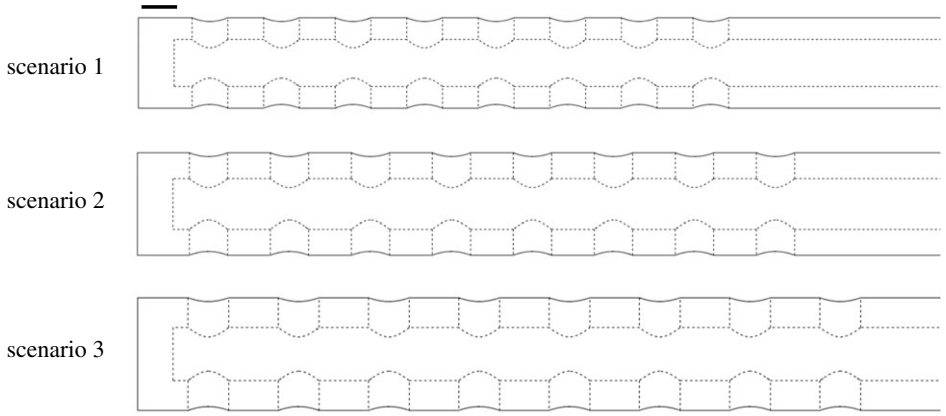

Figure 14. Three different ventricular catheters that share the same dimensionless numbers of $m = 2$, $n = 8$, $\hat{l} = 0.6$ and $\hat{d} = 0.77$. The dimensional geometric parameters of the catheters are given in table 1. Scale bar is 1 mm.

Table 1. Geometric parameters and Reynolds numbers associated with three different scenarios. In all scenarios, *l*/*L* and *d*/*D* were maintained to be 0.6 and 0.77, respectively. All parameters are within a design range in accordance with the range of catheters that have been clinically used [2,26], and the Reynolds number is also within the physiological limit, which is estimated to be 25 (§3.1).

	l (mm)	*L* (mm)	*d* (mm)	*D* (mm)	*Q* (ml min^{-1})	*μ* (mPa s)	*Re*
scenario 1	0.60	1.0	1.00	1.3	0.03	0.8	1
scenario 2	0.72	1.2	1.08	1.4	0.30	0.8	6
scenario 3	0.84	1.4	1.15	1.5	1.00	0.8	18

table 1. It is important to note that matching these dimensionless numbers is different from geometric similarity that requires identical shape across structural models. Provided the result above, we can regard the identified dimensionless numbers as the key design parameters.

4.3. Manipulation of dimensionless numbers to enhance wall shear stress

Here, using CFD and dimensional analysis, we studied how the MWSS levels at holes and lumina can be optimized by adjusting the dimensionless numbers. As we are now interested in the dimensional MWSS values, we re-express (4.1)–(4.3) in their dimensional form:

$$\sum_{i=1}^{k} \tau_i^{\mathcal{H}} = \frac{\hat{l}}{m\hat{d}^4}(\tau_{k+1}^{\mathcal{H}} - \tau_k^{\mathcal{H}}) \quad \text{for } 1 \le k \le n-1, \tag{4.7}$$

$$\sum_{i=1}^{n} \tau_i^{\mathcal{H}} = \frac{\tau_d}{m\hat{d}^3} \tag{4.8}$$

and

$$\tau_k^{\mathcal{L}} = m\hat{d}^3 \sum_{i=1}^{k} \tau_i^{\mathcal{H}} \quad \text{for } 1 \le k \le n, \tag{4.9}$$

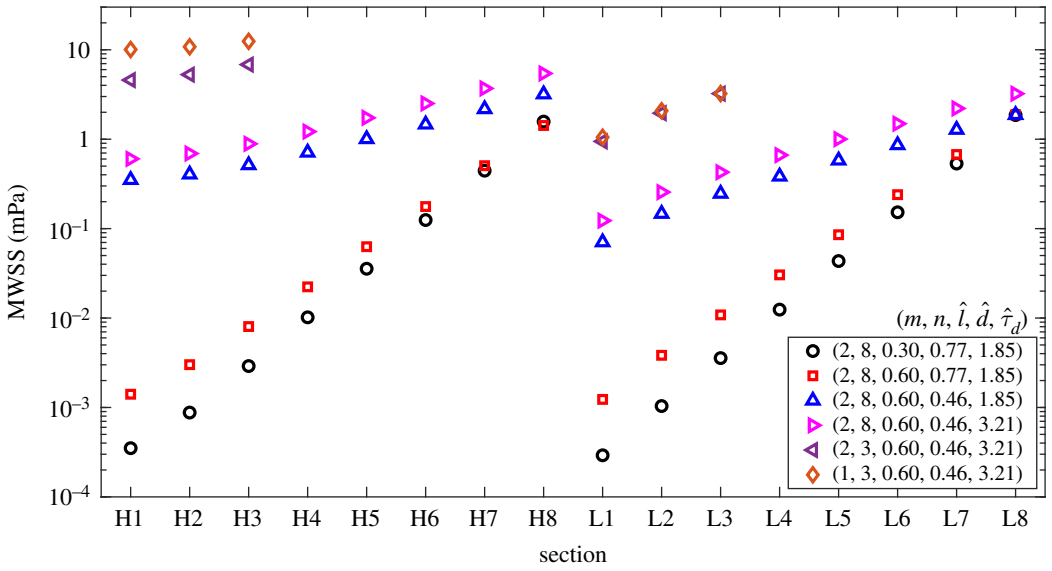

Figure 15. Improving wall shear stress distribution by manipulating a single dimensionless number at a time. All results were obtained from CFD simulations. The total flow rate and CSF viscosity were 0.03 ml min^{-1} and 0.8 mPa s, respectively.

where $\tau_k^{\mathcal{H}}$ and $\tau_k^{\mathcal{L}}$ indicate the MWSS at the kth hole and lumen, respectively. These equations would have the same solution when m, n, $\hat{l}$, $\hat{d}$ and τ_d are kept fixed. For the purpose of dimensional analysis, we introduce another dimensionless number associated with τ_d:

$$\hat{\tau}_d = \tau_d/\tau_c = \frac{32\mu Q}{\pi D^3 \tau_c}, \tag{4.10}$$

where τ_c is the cut-off minimal value of WSS that can inhibit astrocyte growth and adhesion. The value of τ_c is set to 1 mPa in this study.

Using CFD, we show that the MWSS monotonically increases at every section when m, n or $\hat{d}$ decreases or $\hat{\tau}_d$ increases (figure 15). Unlike these straightforward trends, increasing $\hat{l}$ enhanced the value of MWSS of every lumen considered here, but not of every hole. Starting from a geometric model that is not optimized, we optimized the MWSS distribution by controlling a single dimensionless number at a time. During the optimization, we also keep the geometric parameters in a design range that is relevant and consistent with current commercial catheters [2,26]. The geometric parameters of the starting geometry are

$$(m,\ n,\ l,\ L,\ d,\ D) = (2,\ 8,\ 0.6,\ 2.0,\ 1.0,\ 1.3), \tag{4.11}$$

where the unit of l, L, d and D is millimetre. The total flow rate Q was set to 0.03 ml min^{-1} to work with a worst-case scenario with lowest overall wall shear stress, and the viscosity of CSF used was 0.8 mPa s. We measured the viscosity of CSF from human subjects ($n = 37$) as described in detail in electronic supplementary material, S6. We found that the viscosity of CSF typically lies within 0.8–1.8 mPa s at 37°C under 85–1000 s^{-1} of shear rates, where surface tension-induced error [38] is negligible (electronic supplementary material, S6.2). Furthermore, the CSF samples exhibited weak shear thinning with 0.83 ± 0.06 (SD) of the flow behaviour index [39] that was estimated from the data obtained over 85–300 s^{-1}, where slight shear thinning appeared. Here, to consider the worst-case scenario of catheter flow, we use the lowest value of viscosity (i.e. 0.8 mPa s) measured in our human-subject data (electronic supplementary material, S6.1). These parameters then form the set of dimensionless numbers as follows:

$$(m,\ n,\ \hat{l},\ \hat{d},\ \hat{\tau}_d) = (2,\ 8,\ 0.3,\ 0.77,\ 1.85). \tag{4.12}$$

As can be seen in figure 15, we first tested the effect of $\hat{l}$ by increasing its value from 0.3 to 0.6, from the circle to square symbols, while keeping the other dimensionless numbers fixed. Increasing $\hat{l}$ helped optimize the MWSS distribution inside the catheter. Indeed, increasing $\hat{l}$ increased the minimum MWSS of both holes and lumina, i.e. the MWSS increased at H1 and L1. The PNM provides the rationale for such changes. Substituting (4.4) into (4.8) solves for the MWSS at the first hole which is the minimum MWSS across all holes:

$$\tau_1^{\mathcal{H}} = \frac{1}{m\hat{d}^3 \sum_{i=1}^{n} G_i}\tau_d. \tag{4.13}$$

We prove in electronic supplementary material, S5.1, that $\partial \sum_{i=1}^{n} G_i/\partial \hat{l}$ is always negative, which explains why the increase of $\hat{l}$ leads to the increase of $\tau_1^{\mathcal{H}}$.

Now, from (4.4) to (4.13), we obtain

$$\tau_k^{\mathcal{H}} = \frac{G_k}{m\hat{d}^3 \sum_{i=1}^{n} G_i}\tau_d, \tag{4.14}$$

which explains the monotonic increase of the MWSS with hole index, i.e. as we move away from the tip of the catheter toward the valve.

When it comes to the lumen regions (L1–L8), the increased $\hat{l}$ enhanced the MWSS levels in all lumina except for L8 whose MWSS remains unchanged. Plugging (4.14) into equation (4.9) gives

$$\tau_k^{\mathcal{L}} = \frac{\sum_{i=1}^{k} G_i}{\sum_{i=1}^{n} G_i}\tau_d = F_k \tau_d \quad \text{for } 1 \le k \le n, \tag{4.15}$$

which gives $\tau_n^{\mathcal{L}} = \tau_d$, confirming that MWSS at the last lumen does not depend on $\hat{l}$. We also prove in electronic supplementary material, S5.2, that $\partial F_k/\partial \hat{l}$ is positive except for $k = n$, explaining the observed increase of the MWSS at the lumina L1–L7 with the increase of $\hat{l}$.

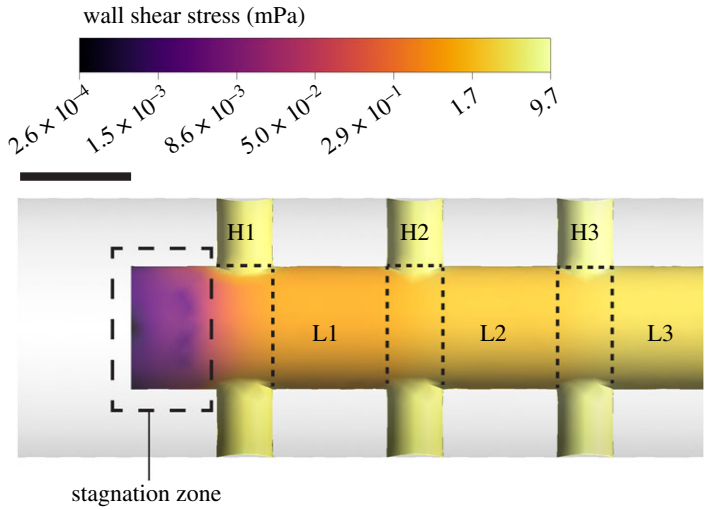

Figure 16. Formation of stagnation zone, revealed by CFD calculations to be near the tip of a typical ventricular catheter, here shown for total system flow rate of $Q = 0.03$ ml min^{-1} and viscosity $\mu = 0.8$ mPa s. The catheter and wall shear stress contour shown here corresponds to the left-pointing triangle markers in figure 15. The stagnation zone has very low wall shear stress, three orders of magnitude lower than 1 mPa, which is the cut-off wall shear stress. Scale bar is 1 mm.

As a next step, we changed $\hat{d}$ from 0.77 to 0.46 (from square to triangle symbols in figure 15), keeping the other dimensionless numbers fixed. Decreasing $\hat{d}$ significantly enhanced the MWSS levels at all sections. This implies $\partial\tau_k^{\mathcal{H}}/\partial\hat{d} < 0$ and $\partial\tau_k^{\mathcal{L}}/\partial\hat{d} < 0$, which are proved in electronic supplementary material, S5.3 and 5.5. Changing $\hat{d}$ has a greater effect on the MWSS distribution, compared with changing other dimensionless numbers. This can be attributed to the high-order nonlinear effect that can be identified in the PNM system (equations (4.7)–(4.9)).

Increasing $\hat{\tau}_d$ raised the MWSS of all sections (from triangle to right-pointing triangle symbols). As τ_d is the non-dimensionalizing factor in the PNM (equations (4.1)–(4.3)), MWSS levels at all sections are simply proportional to $\hat{\tau}_d$. Since designs with different n do not allow the one-to-one comparison across sections, we now compare the minimum MWSS of holes or lumina. $\tau_1^{\mathcal{H}}$ and $\tau_1^{\mathcal{L}}$ are the minimum MWSS across holes and lumina, respectively, according to (4.4) and (4.14). As can be seen in figure 15, decreasing n increases both $\tau_1^{\mathcal{H}}$ and $\tau_1^{\mathcal{L}}$ (from right-point to left-point triangles), since $\sum_{i=1}^{n_1} G_i > \sum_{i=1}^{n_2} G_i$ when $n_1 > n_2$ in (4.13).

$$\tau_1^{\mathcal{H}}|_{n=n_1} < \tau_1^{\mathcal{H}}|_{n=n_2}. \tag{4.16}$$

As $\tau_1^{\mathcal{L}}$, the minimum MWSS across lumina, is equal to $m\hat{d}^3\tau_1^{\mathcal{H}}$ from (4.9), which further extends (4.16) to

$$\tau_1^{\mathcal{L}}|_{n=n_1} < \tau_1^{\mathcal{L}}|_{n=n_2} \quad \text{when } n_1 > n_2. \tag{4.17}$$

Decreasing m enhanced the MWSS levels across all holes and lumina except the final lumen L3 whose MWSS remains fixed. This last result can also be shown using the PNM, deriving that $\partial\tau_k^{\mathcal{H}}/\partial m < 0$ and $\partial\tau_k^{\mathcal{L}}/\partial m \leq 0$ (electronic supplementary material, S5.4 and 5.5).

In sum, in this section, using the CFD and our proposed PNM, we elucidated how dimensionless numbers controlling catheter design should be manipulated to optimize the WSS distribution inside a catheter. The final MWSS distribution, shown with diamond markers in figure 15, has MWSS levels larger than 1 mPa in all sections, meeting optimal threshold condition of minimal adhesion and ease of removal of astrocytes, thus expected minimal flow obstruction potential.

4.4. Formation of stagnation zone at the catheter's tip

Although we showed that the MWSS distribution can be optimized by manipulating the dimensionless numbers, there is still a region which the approach cannot optimize. Indeed, the analysis of §4.3 does not predict the WSS distribution at the surfaces of the region that is shown boxed in figure 16. This region features a stagnation zone, where CSF stagnates and recirculates, inducing very low shear stress on the wall. Based on our results above (§2), this region would be favourable for astrocyte accumulation, allowing for robust adhesion in the region and proliferation that could propagate downstream over time. To avoid this particular stagnation region, in the next section, we propose a new design principle that suppresses such stagnation zone inherent to current ventricular catheter designs.

4.5. A ventricular catheter with open tip-end and its optimization

We suggest a new geometry whose tip has an aperture with a depth of L_e (figure 17*a*). The newly formed aperture is now called L0. Using a similar argument given in the derivation of the PNM for typical ventricular catheters, we can introduce another PNM to take the new aperture into account:

$$\tau_0^{\mathcal{L}} = \frac{\hat{l}_e}{\hat{d}}\tau_1^{\mathcal{H}}, \tag{4.18}$$

$$\sum_{i=1}^{k}\tau_i^{\mathcal{H}} = \frac{\hat{l}}{m\hat{d}^4}\left(\tau_{k+1}^{\mathcal{H}} - \tau_k^{\mathcal{H}} - \frac{\hat{d}}{\hat{l}}\tau_0^{\mathcal{L}}\right) \quad \text{for } 1 \leq k \leq n-1, \tag{4.19}$$

$$\sum_{i=1}^{n}\tau_i^{\mathcal{H}} = \frac{\tau_d - \tau_0^{\mathcal{L}}}{m\hat{d}^3} \tag{4.20}$$

and

$$\tau_k^{\mathcal{L}} = \tau_0^{\mathcal{L}} + m\hat{d}^3\sum_{i=1}^{k}\tau_i^{\mathcal{H}} \quad \text{for} \quad 1 \leq k \leq n, \tag{4.21}$$

where $\hat{l}_e = l/L_e$ and the other variables are defined as in the previous model (equations (4.7)–(4.9)). The above system of linear equations gives the MWSS levels at all sections including the newly added aperture L0. Using this model, we solved a numerical optimization problem that maximizes

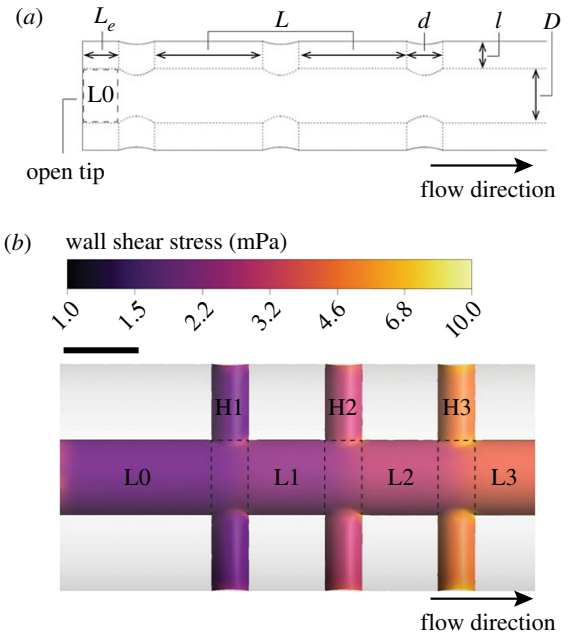

Figure 17. (*a*) Geometric parameters involved in designing a novel catheter with open tip end discussed in §4.4. (*b*) WSS heat-map of the catheter with such open end optimized for all MWSS values to be larger than 1 mPa, i.e. meeting the threshold condition of low proliferation and adhesion of astrocytes. Scale bar is 1 mm.

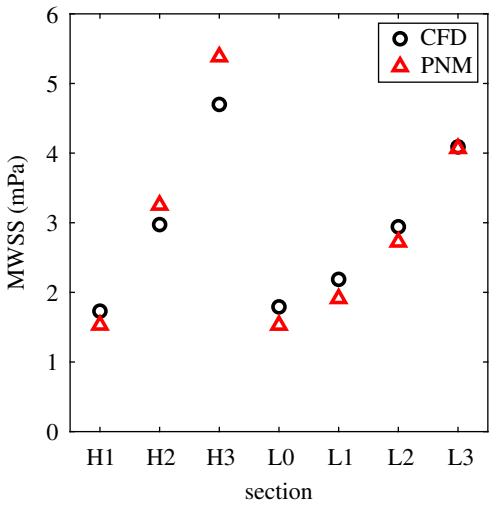

Figure 18. MWSS value distribution formed in an optimized catheter with open tip end (§4.4), all maintained above the 1 mPa threshold above which low proliferation and adhesion of astrocytes are expected. An error between the MWSS level from the CFD and PNM at a section is less than 16%, where the error is quantified by $|MWSS_{PNM} - MWSS_{CFD}|/MWSS_{CFD}$.

the minimum MWSS across all sections L0–L3 and H1–H3. Here, we also assumed that the total flow rate is 0.03 ml min^{-1} and the viscosity of CSF is 0.8 mPa s. In this example of optimization of an open-ended catheter, without loss of generality, the parameters m and n were fixed to 2 and 3, respectively. The input variables of the optimization were the length of the end open region, L_e, hole spacing L, hole diameter d, hole depth l and lumen diameter D, which is illustrated in figure 17. Given that the PNM calculates the wall shear stress distribution more than a hundred times faster than the CFD simulation, we use the PNM for optimization. Coupling the modified PNM to an interior-point approach to constrained minimization (e.g. the fmincon function in MATLAB), we compute the optimal geometry with constrained upper and lower bounds of the geometric parameters to remain within the range of values of commercial catheters [2,26]. In addition to the bound constraints, additional geometric constraints imposed are: (1) D cannot be smaller than d, which is an inherent geometric constraint; and (2) L cannot be smaller than d, which ensures efficacy of the PNM which assumes fully developed flow in lumina regions.

As can be seen in the computational (CFD) results of figure 17*b*, for $Q = 0.03$ ml min^{-1}, the optimal solution shows MWSS values larger than 1 mPa for every inner surface, with no stagnation zone. The PNM calculation also shows a good agreement with that from the CFD analysis (figure 18), confirming again that the PNM can be used instead of CFD to design optimized ventricular catheters while ensuring not only fast computation but also accuracy.

5. Discussion

Hydrocephalus involves enlarged cerebral ventricles due to excess CSF in the cerebral ventricular system. Ventricular catheters have had great success in alleviating this condition. However, they have a low lifespan due to obstruction, with 60% failure rate within 2 years. The obstruction is caused in large part by glial tissue ingrowth, consisting mainly of astrocytes and microglia. These two cell types populate the catheter at different timescales, with early migration by microglia and later dominance by astrocytes. Improving the shunt lifespan by years particularly requires prevention of the astrocyte-dominant tissue formation since astrocytes are most frequently found in catheters explanted for late shunt failures (greater than two months). We focused this study on elucidating the long-term fluid shear stress effect on astrocytes in the context of the obstruction of ventricular catheters and used our findings to propose a systematic and efficient method of optimization of ventricular catheter designs that can alleviate the adhesion and proliferation of these cells, thus potentially addressing one family of obstructions. To do so, we conducted *in vitro* cultures of astrocytes in microfluidic channels, mimicking glial tissue formation in ventricular catheters. We discovered that long-term fluid shear stress decreases confluency and increases loss of their star-like morphology. Furthermore, the long-term fluid shear stress facilitated the forced detachment by suddenly imposed high fluid shear stress that could be encountered during regular changes of position of patients, coughs, that result in shunt-valve opening. Our results offer fundamental insights into an approach for geometric optimization of the design of ventricular catheter intended to minimize astrocyte-induced obstructions.

The underlying mechanism governing the observed behaviour of astrocytes upon long-term shear fluid stress remains to be confirmed. The literature suggests that it may be governed by mechano-sensitive calcium channels on the cell membrane. Indeed, Charles *et al.* [40] found that mechanical poking to rat glial cells results in increased measured calcium levels in the poked glial cell and also generates calcium waves from the poked cell to neighbouring cells. More recently, Maneshi *et al.* [41] identified the type of calcium channels that causes calcium entry into rat astrocytes upon fluid shear stress shock. Given this mechano-sensitive calcium channel of astrocytes, it is also known that calcium

overload in glial cells can trigger their death [42–44]. These prior results coupled with our results suggest that long-term fluid shear stress may induce prolonged opening of astrocyte calcium channels, leading to a disturbed homeostasis of their cytosolic calcium level, ultimately causing decrease in their confluency and loss of their typical star-like morphology. Note that our results on cytotoxicity of fluid shear stress to astrocytes were derived using culture of a single cell type.

From detailed analyses of explanted catheters, it is known that microglia first migrate to the catheter and astrocytes form glial tissue thereafter [9,10]. Given that microglia have been found to support the function of astrocytes in multiple immunological contexts [45,46], investigating the response of a co-culture system of astrocytes and microglia under shear flow would be a valuable next objective to more precisely understand the obstruction by astrocytic glial tissue. Also, studying the activity of glial cells under long-term shear flow, such as identifying associated gene expression profiles, would enable us to further characterize the biological state of glial cells in response to persistent shear flow. The results presented in this study are a baseline for future studies considering additional complexity and factors from co-culturing with microglia to preconditioning astrocytes to a biochemical state that relates to a specific pathological condition.

Lin *et al.* [37] first reported that typical ventricular catheter designs exceedingly concentrate flow at the most downstream set of holes. The authors hypothesized that the elevated flow through these holes can elevate the probability of blockages at these holes and that their obstruction may extend to the luminal part of the catheter and thereby disable the entire catheter at once. In support of their hypothesis, the authors state that obstructing tissue is found most frequently around the most downstream set of holes in explanted catheters, yet clear evidence for this claim is currently lacking. However, based on this hypothesis, multiple studies have attempted to homogenize the flow rate distribution across catheter holes by changing the catheter hole geometry [29,37,47] in an effort to decrease the probability of aspirating bulk tissue and cells at a given hole. By contrast, based on the response of astrocytes to long-term shear flow, we set the design objective for ventricular catheters to maximizing wall shear stress across the inner surfaces of a catheter. This objective is fundamentally different from the objective of the prior studies on catheter design optimization that focused on homogenizing flow rate distribution across holes. Indeed, we established another goal for designing ventricular catheters, particularly related to the obstruction by astrocytes: *enhancing the wall shear stress inside a ventricular catheter*. It is important to note that this goal is not necessarily attained by homogenizing the flow rate distribution. According to the PNM, τ_H^i is scaled by Q_H^i/d_i^3, where Q_H^i and d_i are the flow rate and diameter of the ith hole, respectively. This scaling implies that a geometry that has equally distributed flow rates can fail to achieve the minimal value of wall shear stress across a hole that hinders astrocyte obstruction, due to hole diameters that are chosen to be too large. Our PNM for ventricular catheters can also be used for the exploration of a range of viable design principles that seek to achieve multiple design objectives regarding the catheter flow. For example, one may be interested in wall shear stress maximization and also flow rate homogenization across holes. Such a solution can be obtained, as illustrated in electronic supplementary material, S7, by coupling the PNM with a multi-objective genetic algorithm [48]. Moreover, the lumped-element approach of the PNM enables exploration of designs whose hole depths, hole spacing, and hole diameters are not constant, allowing us to explore flow optimization in a large parameter space [49].

This study tackles how astrocytes attached on the catheter surface respond to long-term fluid shear stress. It does not address the mechanism of initial migration of astrocytes to the catheter. Harris & McAllister [50] conducted bioreactor experiments that exposed different catheter models to an astrocyte suspension. The authors sought to address the effect of hole size on the adhesion of astrocytes from the liquid suspension. Their study shows that the smaller the catheter hole (and the higher the computed wall shear stress), the higher the number of astrocytes that adhere to the hole surface. Our work here appears to contradict the results obtained by Harris & McAllister [50]. However, CFD simulations of their catheter designs, including the effect of taper of the catheter holes that are evident from fig. 5 in Harris & McAllister [50], demonstrate that their calculated wall shear stress for the smaller catheter holes when ignoring the taper is an overestimate of the average wall shear stress across holes when taking the taper into account. When accounting for the taper, the catheters with the smaller holes have smaller wall shear stress values compared to those with larger holes. Detailed simulations of the shunt flow through holes of different size and taper might be required to understand further how wall shear stress is affected by various design parameters.

Lastly, we suggest that the introduction of bulk tissue, such as choroid plexus, to a hole can form low wall shear stress zones at the hole surface. Our preliminary CFD results given in electronic supplementary material, S8, show that a partially blocked hole results in local regions where wall shear stress is lower than that of the unblocked control case. This result implies that astrocytes may grow in the regions of low wall shear stress, filling the spatial gap between the blocking tissue and the hole surface. This hypothesis aligns with the observations by Hanak *et al.* [10] that astrocytes are found between the catheter surface and bulk tissue.

In sum, using a microfluidic culture system, we showed that astrocytes are vulnerable to long-term fluid shear stress. Based on this insight, and having experimentally confirmed Poiseulle-type flow in the catheter, we developed a physics-based PNM to guide optimization of the geometric parameters to enhance wall shear stress inside typical ventricular catheters in addition to a design principle that suppresses a potentially nefarious flow stagnation zone which is commonly formed in current typical ventricular catheters. The design principles [49] provided in this study are expected to extend the lifespan of ventricular catheters and enhance the quality of life of hydrocephalus patients.

Data accessibility. The key experimental and numerical data are all given in the article and electronic supplementary material.

Authors' contributions. S.L. carried out the laboratory work, data collection and analysis, clinical sample analysis, the theoretical and numerical computations, participated in the design of the study and drafted and revised the manuscript; N.K. carried out initial explorations of the microscopy and CFD simulations; J.H. supervised clinical data collection and critically revised the manuscript; T.H. and L.B. conceived of the study, designed the study, supervised the study, coordinated the study and helped draft and revise the manuscript. All authors gave final approval for publication and agree to be held accountable for the work performed therein.

Competing interests. We declare we have no competing interests.

Funding. We thank the Edgerton Fund and the MIT Research Committee Funds (Reed, Ferry and Westaway) for partially supporting this work. S.L. thanks the Kwanjeong Educational Foundation Scholarship for partial financial support.

Acknowledgements. S.L. thanks Raj Dandekar at Bourouiba Group and Tak Ko at Picower Institute for valuable discussions. The authors wish to thank Leewon Seo for help with illustrating the shunt system and Dr Michael D. Perloff, Brandon Finn, Helena Lau, and Dr Sherida Padilla at Boston Medical Center for help with obtaining the CSF samples.

References

1. Pople IK. 2002 Hydrocephalus and shunts: what the neurologist should know. *J. Neurol. Neurosurg. Psychiatry* **73**(suppl 1), i17–i22. (doi:10.1136/jnnp.73.suppl_1.i17)
2. Drake JM, Sainte-Rose C. 1995 *The shunt book*. Oxford, UK: Blackwell Science.
3. Paff M, Alexandru-Abrams D, Muhonen M, Loudon W. 2018 Ventriculoperitoneal shunt complications: a review. *Interdiscip. Neurosurg.* **13**, 66–70. (doi:10.1016/j.inat.2018.04.004)
4. Stone JJ, Walker CT, Jacobson M, Phillips V, Silberstein HJ. 2013 Revision rate of pediatric ventriculoperitoneal shunts after 15 years. *J. Neurosurg. Pediatr.* **11**, 15–19. (doi:10.3171/2012.9.PEDS1298)
5. Iskandar BJ, Tubbs S, Mapstone TB, Grabb PA, Bartolucci AA, Oakes WJ. 1998 Death in shunted hydrocephalic children in the 1990s. *Pediatr. Neurosurg.* **28**, 173–176. (doi:10.1159/000028644)
6. Punt J, Buxton N. 1998 Failure to follow patients with hydrocephalus shunts can lead to death. *Br. J. Neurosurg.* **12**, 399–401. (doi:10.1080/02688699844574)
7. Lazareff J, Peacock W, Holly L, Ver Halen J, Wong A, Olmstead C. 1998 Multiple shunt failures: an analysis of relevant factors. *Childs Nerv. Syst.* **14**, 271–275. (doi:10.1007/s003810050223)
8. Hanak BW, Bonow RH, Harris CA, Browd SR. 2017 Cerebrospinal fluid shunting complications in children. *Pediatr. Neurosurg.* **52**, 381–400. (doi:10.1159/000452840)
9. Sarkiss CA, Sarkar R, Yong W, Lazareff JA. 2014 Time dependent pattern of cellular characteristics causing ventriculoperitoneal shunt failure in children. *Clin. Neurol. Neurosurg.* **127**, 30–32. (doi:10.1016/j.clineuro.2014.09.029)
10. Hanak BW, Ross EF, Harris CA, Browd SR, Shain W. 2016 Toward a better understanding of the cellular basis for cerebrospinal fluid shunt obstruction: report on the construction of a bank of explanted hydrocephalus devices. *J. Neurosurg. Pediatr.* **18**, 213–223. (doi:10.3171/2016.2.PEDS15531)
11. Salatino JW, Ludwig KA, Kozai TD, Purcell EK. 2017 Glial responses to implanted electrodes in the brain. *Nat. Biomed. Eng.* **1**, 862–877. (doi:10.1038/s41551-017-0154-1)
12. Cornelison RC, Kingsmore KM, Brennan CE, Tom S, Munson JM. 2018 Characterizing interstitial fluid flow and the effects of shear stress in the brain tumor microenvironment. In *2018 AIChE Annual Meeting, Pittsburgh, PA, USA, 28 October–2 November 2018*. New York, NY: AIChE.
13. Fischer I, Alliod C, Martinier N, Newcombe J, Brana C, Pouly S. 2011 Sphingosine kinase 1 and sphingosine 1-phosphate receptor 3 are functionally upregulated on astrocytes under pro-inflammatory conditions. *PLoS ONE* **6**, e23905. (doi:10.1371/journal.pone.0023905)
14. Wanner IB, Anderson MA, Song B, Levine J, Fernandez A, Gray-Thompson Z, Ao Y, Sofroniew MV. 2013 Glial scar borders are formed by newly proliferated, elongated astrocytes that interact to corral inflammatory and fibrotic cells via stat3-dependent mechanisms after spinal cord injury. *J. Neurosci.* **33**, 12 870–12 886. (doi:10.1523/JNEUROSCI.2121-13.2013)
15. Harris C, Pearson K, Hadley K, Zhu S, Browd S, Hanak BW, Shain W. 2015 Fabrication of three-dimensional hydrogel scaffolds for modeling shunt failure by tissue obstruction in hydrocephalus. *Fluids Barriers CNS* **12**, 26. (doi:10.1186/s12987-015-0023-9)
16. Integra LifeSciences. Codman external drainage ventricular catheter set. See https://www.integralife.com (accessed 16 August 2019).
17. Phelan K, May KM. 2015 Basic techniques in mammalian cell tissue culture. *Curr. Protoc. Cell Biol.* **66**, 1–1. (doi:10.1002/0471143030.cb0101s36)
18. ibidi GMBH. μ-Slide I luer. See https://ibidi.com/channel-slides/50–slide-i-luer.html (accessed 26 September 2019).
19. Wilhelmsson U, Bushong EA, Price DL, Smarr BL, Phung V, Terada M, Ellisman MH, Pekny M. 2006 Redefining the concept of reactive astrocytes as cells that remain within their unique domains upon reaction to injury. *Proc. Natl Acad. Sci. USA* **103**, 17 513–17 518. (doi:10.1073/pnas.0602841103)
20. Jaccard N, Griffin LD, Keser A, Macown RJ, Super A, Veraitch FS, Szita N. 2014 Automated method for the rapid and precise estimation of adherent cell culture characteristics from phase contrast microscopy images. *Biotechnol. Bioeng.* **111**, 504–517. (doi:10.1002/bit.25115)
21. Thomas R, Salter MG, Wilke S, Husen A, Allcock N, Nivison M, Nnoli AN, Fern R. 2004 Acute ischemic injury of astrocytes is mediated by Na-K-Cl cotransport and not Ca^{2+} influx at a key point in white matter development. *J. Neuropathol. Exp. Neurol.* **63**, 856–871. (doi:10.1093/jnen/63.8.856)
22. Tynan RJ, Beynon SB, Hinwood M, Johnson SJ, Nilsson M, Woods JJ, Walker FR. 2013 Chronic stress-induced disruption of the astrocyte network is driven by structural atrophy and not loss of astrocytes. *Acta Neuropathol.* **126**, 75–91. (doi:10.1007/s00401-013-1102-0)
23. Kulijewicz-Nawrot M, Verkhratsky A, Chvatal A, Sykova E, Rodríguez JJ. 2012 Astrocytic cytoskeletal atrophy in the medial prefrontal cortex of a triple transgenic mouse model of Alzheimer's disease. *J. Anat.* **221**, 252–262. (doi:10.1111/j.1469-7580.2012.01536.x)
24. Diniz LP *et al.* 2017 Astrocyte transforming growth factor beta 1 protects synapses against Aβ oligomers in Alzheimer's disease model. *J. Neurosci.* **37**, 6797–6809. (doi:10.1523/JNEUROSCI.3351-16.2017)
25. Gehlen M, Eklund A, Kurtcuoglu V, Malm J, Daners MS. 2017 Comparison of anti-siphon devices—how do they affect CSF dynamics in supine and upright posture? *Acta Neurochir. (Wien)* **159**, 1389–1397. (doi:10.1007/s00701-017-3249-2)
26. Medtronic. *Neurosurgery product catalog*. See http://video.medtronic.com/neuro/neuro_product_catalog/ (accessed 13 May 2020).
27. Klose U, Strik C, Kiefer C, Grodd W. 2000 Detection of a relation between respiration and CSF pulsation with an echoplanar technique. *J. Magn. Reson. Imaging* **11**, 438–444. (doi:10.1016/j.inat.2018.04.004)
28. Hara M, Kadowaki C, Konishi Y, Ogashiwa M, Numoto M, Takeuchi K. 1983 A new method for measuring cerebrospinal fluid flow in shunts. *J. Neurosurg.* **58**, 557–561. (doi:10.3171/jns.1983.58.4.0557)
29. Weisenberg SH, TerMaath SC, Barbier CN, Hill JC, Killeffer JA. 2018 A computational fluid dynamics simulation framework for ventricular catheter design optimization. *J. Neurosurg.* **129**, 1067–1077. (doi:10.3171/2017.5.JNS161882)
30. Lui AC, Polis TZ, Cicutti NJ. 1998 Densities of cerebrospinal fluid and spinal anaesthetic solutions in surgical patients at body temperature. *Can. J. Anaesth.* **45**, 297. (doi:10.1007/BF03012018)
31. Bloomfield I, Johnston I, Bilston L. 1998 Effects of proteins, blood cells and glucose on the viscosity of cerebrospinal fluid. *Pediatr. Neurosurg.* **28**, 246–251. (doi:10.1159/000028659)
32. Brinker T, Stopa E, Morrison J, Klinge P. 2014 A new look at cerebrospinal fluid circulation. *Fluids Barriers CNS* **11**, 10. (doi:10.1186/2045-8118-11-10)
33. Lee S. 2019 Flow optimization of ventricular catheters for shear stress-induced death of astrocytes. Master's thesis, Massachusetts Institute of Technology.
34. Saksena R, Christensen KT, Pearlstein AJ. 2015 Surrogate immiscible liquid pairs with refractive indexes matchable over a wide range of density and viscosity ratios. *Phys. Fluids* **27**, 087103. (doi:10.1063/1.4928030)
35. Kundu PK, Dowling DR, Tryggvason G, Cohen IM. 2016 *Fluid mechanics*. New York, NY: Academic Press.

36. Sparrow EM, Anderson C. 1977 Effect of upstream flow processes on hydrodynamic development in a duct. *ASME Trans. I-J. Fluids Eng.* **99**, 556–560. (doi:10.1115/1.3448846)
37. Lin J, Morris M, Olivero W, Boop F, Sanford RA. 2003 Computational and experimental study of proximal flow in ventricular catheters. *J. Neurosurg.* **99**, 426–431. (doi:10.3171/jns.2003.99.2.0426)
38. Ewoldt RH, Johnston MT, Caretta LM. 2015 Experimental challenges of shear rheology: how to avoid bad data. In *Complex fluids in biological systems*, pp. 207–241. Berlin, Germany: Springer. (doi:10.1007/978-1-4939-2065-5_6).
39. Ostwald W. 1925 Ueber die Geschwindigkeitsfunktion der Viskosität disperser Systeme. I. *Colloid Polym. Sci.* **36**, 99–117. (doi:10.1007/BF01431449)
40. Charles AC, Merrill JE, Dirksen ER, Sandersont MJ. 1991 Intercellular signaling in glial cells: calcium waves and oscillations in response to mechanical stimulation and glutamate. *Neuron* **6**, 983–992. (doi:10.1016/0896-6273(91)90238-U)
41. Maneshi MM, Maki B, Gnanasambandam R, Belin S, Popescu GK, Sachs F, Hua SZ. 2017 Mechanical stress activates NMDA receptors in the absence of agonists. *Sci. Rep.* **7**, 39610. (doi:10.1038/srep39610)
42. Alberdi E, Sánchez-Gómez MV, Matute C. 2005 Calcium and glial cell death. *Cell Calcium* **38**, 417–425. (doi:10.1016/j.ceca.2005.06.020)
43. Matute C. 2010 Calcium dyshomeostasis in white matter pathology. *Cell Calcium* **47**, 150–157. (doi:10.1016/j.ceca.2009.12.004)
44. Then C, Liu K, Liao M, Chung K, Wang J, Shen S. 2017 Antidepressants, sertraline and paroxetine, increase calcium influx and induce mitochondrial damage-mediated apoptosis of astrocytes. *Oncotarget* **8**, 115490. (doi:10.18632/oncotarget.23302)
45. Zhang D, Hu X, Qian L, O'Callaghan JP, Hong J-S. 2010 Astrogliosis in CNS pathologies: is there a role for microglia? *Mol. Neurobiol.* **41**, 232–241. (doi:10.1007/s12035-010-8098-4)
46. Liddelow SA *et al.* 2017 Neurotoxic reactive astrocytes are induced by activated microglia. *Nature* **541**, 481–487. (doi:10.1038/nature21029)
47. Galarza M, Giménez Á, Valero J, Pellicer OP, Amigó JM. 2014 Computational fluid dynamics of ventricular catheters used for the treatment of hydrocephalus: a 3D analysis. *Childs Nerv. Syst.* **30**, 105–116. (doi:10.1007/s00381-013-2226-1)
48. Deb K. 2001 *Multi-objective optimization using evolutionary algorithms*, vol. 16. New York, NY: John Wiley & Sons.
49. Bourouiba L, Lee S, Heldt T. 2019 Cerebrospinal fluid space draining catheters. US and PCT provisional patent application filed on 20 November 2019.
50. Harris CA, McAllister JP. 2011 Does drainage hole size influence adhesion on ventricular catheters? *Childs Nerv. Syst.* **27**, 1221–1232. (doi:10.1007/s00381-011-1430-0)

Supplementary materials – Enhanced wall shear stress prevents obstruction by astrocytes in ventricular catheters

S. Lee[1], N. Kwok[2], J. Holsapple[3], T. Heldt[2,4], and L. Bourouiba[1,2,4,*]

[1]The Fluid Dynamics of Disease Transmission Laboratory, MIT, Cambridge, MA 02139, USA
[2]Health Sciences & Technology Program, Harvard Medical School, Boston, MA 02115, USA
[3]Department of Neurosurgery, Boston Medical Center, Boston, MA 02118, USA
[4]Institute for Medical Engineering and Science, MIT, Cambridge, MA 02139, USA
[*]lbouro@mit.edu

1 Poiseuille flows in ventricular catheters

We first offer detailed velocity profiles at catheter holes discussed in §4.1 to validate the profile and the simulations and theory that are then subsequently used. Figure S1 show the 2D velocity profiles at the hole at different plane depths (or z-slices). As can be seen in the figure, both profiles from CFD simulation and Poiseuille theoretical calculation are in excellent agreement with the experimental data across all slices of visualizations. A detailed description of the experimental method is given in Figure S2. Using CFD simulations, we also found Poiseuille flows at both holes and lumina, at Re = 25 – the upper limit of the catheter flow regime – (Fig. S3).

2 Derivation of Poiseuille network model for typical ventricular catheters

Here, a Poiseuille network model (PNM) is proposed to estimate the flow rate and wall shear stress (WSS) distributions along holes and lumina (Fig. S4). The model formulates a typical ventricular catheter as a multiple-pipe system that has multiple CSF-diverting holes along the lateral direction. Given §4.1 and §S-1, Poiseuille's law is assumed across all holes and lumina.

Suppose a ventricular catheter has n number of segments. Figure S4 shows the k^{th} and $(k+1)^{th}$ holes that are connected by the k^{th} lumen. Every hole of the catheter has a diameter d and depth l. We assume that the holes at a segment are arrayed symmetrically so that they have the same flow rate Q_k. Every lumen has diameter D and length L. Assume o to be a point source of CSF. Given the total head at point o is h_o, the total head at point 3 can be calculated in two ways.

$$h_3 = h_o + (h_{o\to1} + h_{1\to4} + h_{4\to3}) = h_o + (h_{o\to2} + h_{2\to3}) \tag{S.1}$$

The change of the total head along each path is the sum of frictional loss h^f and the change of elevation head. Since the change of elevation head along the two paths are equal to one another, the paths should have the same h^f.

$$h^f_{o\to1} + h^f_{1\to4} + h^f_{4\to3} = h^f_{o\to2} + h^f_{2\to3}. \tag{S.2}$$

The frictional loss from point o to both point 1 and 2 is negligible, for no ventricular wall effect is assumed. This leads to

$$h^f_{1\to4} + h^f_{4\to3} = h^f_{2\to3}. \tag{S.3}$$

Applying Poiseuille's law to estimate frictional loss, we obtain

$$\left(\frac{l}{d^4}\right)Q_k + \sum_{i=1}^{k}\left[\left(\frac{mL}{D^4}\right)Q_i\right] = \left(\frac{l}{d^4}\right)Q_{k+1}, \qquad k = 1,2,\cdots,(n-1). \tag{S.4}$$

The total flow rate Q is equal to the sum of all flow rates.

$$\sum_{i=1}^{n} mQ_i = Q. \tag{S.5}$$

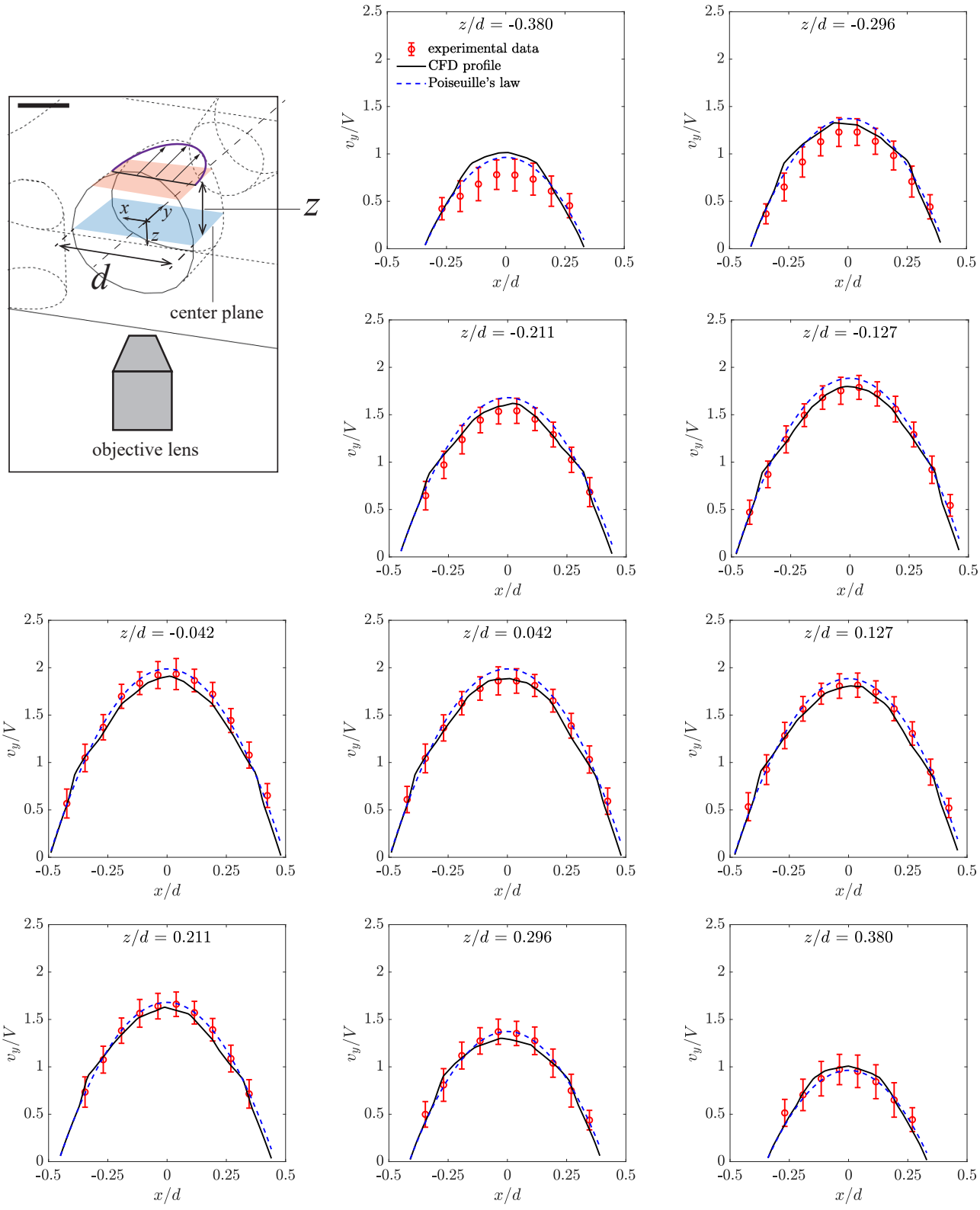

Figure S1. 2D velocity profiles at the catheter holes discussed in §4.1. Each point of the experimental data is the mean value of measured velocities of fluorescent particles whose x-position are within $\pm 0.039d$ from the x-position of the point. Error bars reflect the standard deviation over the measured velocities whose n is larger than 30. The theoretical Poiseuille profiles are chosen to match the flow rate measured by the experiment. The CFD profiles are from the simulation where the flow rate at the catheter outlet matches that of the experiment. The flow rate calculated by CFD was 1.012 times higher than that estimated by the direct experimental measurements. Scale bar in the first top-left panel is 0.5 mm.

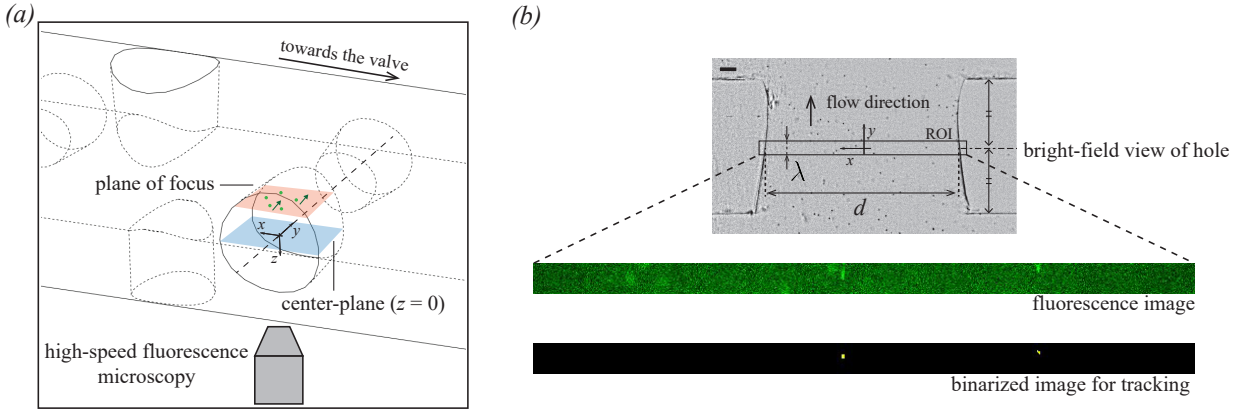

Figure S2. (a) Schematic of experimental setup for 3D velocity profile measurement. Layered imaging was performed by changing the z-location of the plane of focus. 5 μm green fluorescent particles (G0500, ThermoFisher) were used for flow visualization. (b) Region of interest (ROI) with the width $d = 1180$ μm and height $\lambda = 60$ μm was recorded to obtain the velocity profile. λ was set to 7% of the hole depth to ensure both the accuracy of velocity measurement and the use of the highest sampling rate of the microscope. Fluorescence image was binarized by a contrast-thresholding technique in order to selectively extract particles that are in focus. The binarized image was fed into our in-house particle tracking code to estimate the particle velocity. Live video is also available in Movie S3. Scale bar is 100 μm.

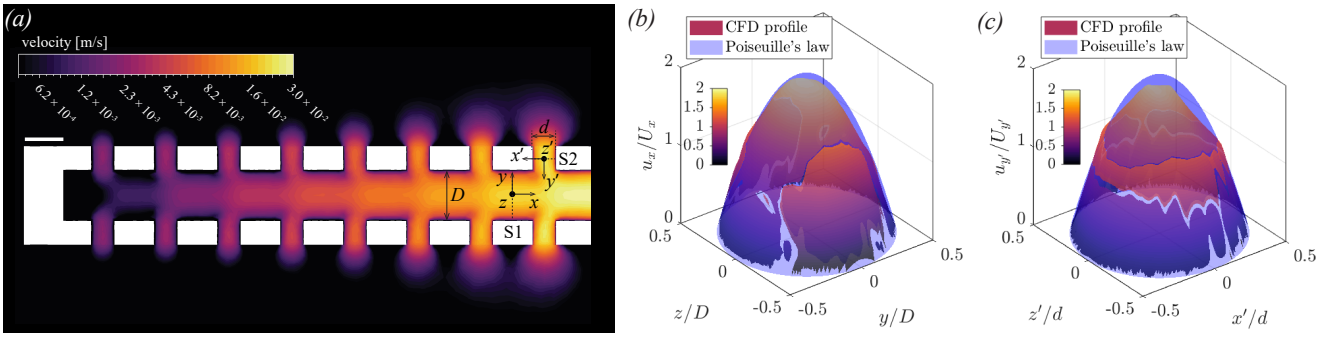

Figure S3. CFD simulation of flow in a ventricular catheter with the configuration of the upward-pointing triangle markers of Figure 15. The Reynolds number is 25 (§3) – the higher value expected in these catheter systems. (a) Velocity field at the catheter middle plane. Flows are pre-developed from the outside of the holes, as confirmed in our experiment (Fig. 11). Scale bar is 1 mm. At the cross-sections S1 and S2, where the local Reynolds numbers of lumina and hole are maximized, respectively, we find the following. (b) The CFD profile at the cross-section S1 is very well captured by a Poiseuille with 6% error. (c) The CFD profile at S2 is also in agreement with the Poiseuille profile with 9% error. Here, U_x, $U_{y'}$ are the mean velocities at S1 and S2, respectively. For both cross-sections, we use the same flow rate for the Poiseuille profiles and in the corresponding CFD calculation. Here, we define the error as $\frac{\|\mathbf{v}_{\text{Poiseuille}} - \mathbf{v}_{\text{CFD}}\|_2}{\|\mathbf{v}_{\text{CFD}}\|_2}$, analogous to what we used in §4.1
.

Solving equations (S.4) and (S.5) together gives the flow rate distribution.

From Poiseuille's law, we have

$$Q_k = \frac{\pi d^3}{32\mu}\tau_k^{\mathscr{H}}, \tag{S.6}$$

where μ is the viscosity of CSF and $\tau_k^{\mathscr{H}}$ is the mean wall shear stress at the k^{th} hole. For the flow rate at the k^{th} lumen is $\sum_{i=1}^{k} mQ_i$, the mean wall shear stress at the lumen is

$$\tau_k^{\mathscr{L}} = \frac{32\mu}{\pi D^3}\sum_{i=1}^{k} mQ_i = m\hat{d}^{\,3}\sum_{i=1}^{k}\tau_i^{\mathscr{H}}, \quad \text{where } \hat{d} = d/D. \tag{S.7}$$

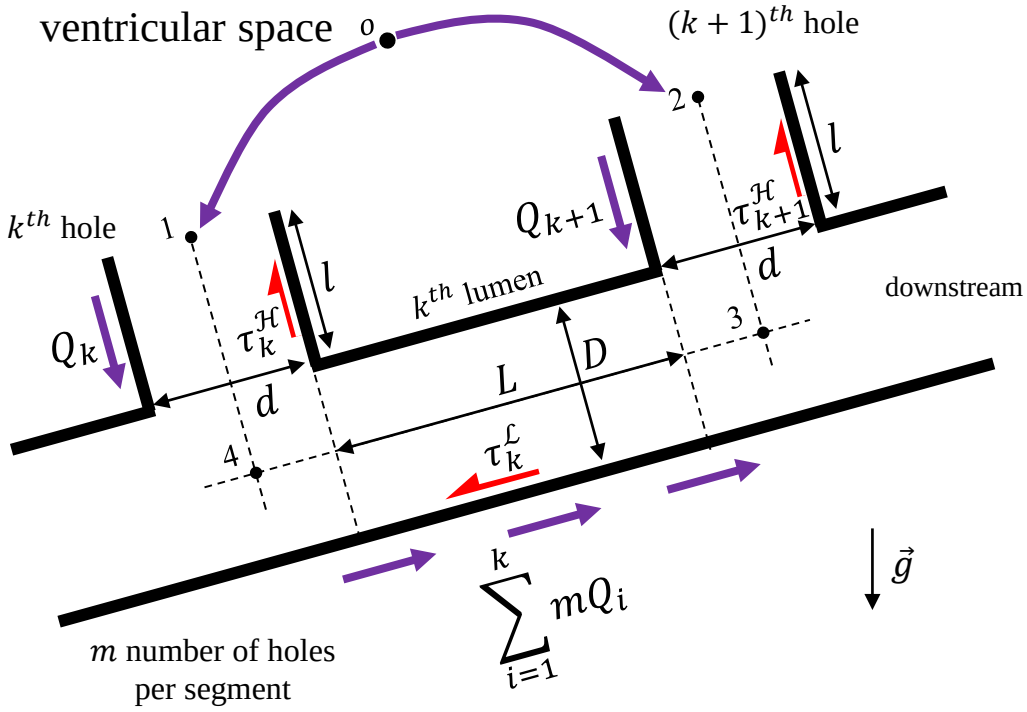

Figure S4. Schematic of the Poiseuille network model (PNM) proposed herein.

Plugging equation (S.6) into equation (S.4) gives

$$\sum_{i=1}^{k} \tau_i^{\mathscr{H}} = \frac{\hat{l}}{m\hat{d}^4}\left(\tau_{k+1}^{\mathscr{H}} - \tau_k^{\mathscr{H}}\right), \quad \text{where } \hat{l} = l/L. \tag{S.8}$$

Finally, substituting (S.6) into (S.5) leads to

$$\sum_{i=1}^{n} \tau_i^{\mathscr{H}} = \frac{\tau_d}{m\hat{d}^3}, \quad \text{where } \tau_d = \frac{32\mu Q}{\pi D^3}. \tag{S.9}$$

Equations (S.7) – (S.9) complete the Poiseuille network model for the typical ventricular catheter.

Now, we want to obtain the explicit formula of the wall shear stress sequence defined by equation (S.8). Suppose $\tau_k^{\mathscr{H}} = G_k \tau_1^{\mathscr{H}}$. For $k = j-1$ and $k = j$, we obtain the following equations from (S.8).

$$G_1 + G_2 + \cdots + G_{j-1} = \frac{1}{c}(G_j - G_{j-1}), \tag{S.10}$$

$$G_1 + G_2 + \cdots + G_{j-1} + G_j = \frac{1}{c}(G_{j+1} - G_j), \quad \text{where } c = \frac{m\hat{d}^4}{\hat{l}}. \tag{S.11}$$

Subtracting (S.10) from (S.11) gives

$$G_{j+1} - (c+2)G_j + G_{j-1} = 0. \tag{S.12}$$

We assume the explicit formula for G_k follows

$$G_k = A\alpha^{k-1} + B\beta^{k-1}. \tag{S.13}$$

Given $G_1 = 1$ and $G_2 = c + 1$, plugging (S.13) into (S.12) allows us to find A, B, α, and β as follows

$$A = \frac{1}{2} + \frac{c}{2\sqrt{c^2+4c}}, \tag{S.14}$$

$$\alpha = 1 + \frac{c+\sqrt{c^2+4c}}{2}, \tag{S.15}$$

$$B = \frac{1}{2} - \frac{c}{2\sqrt{c^2+4c}}, \tag{S.16}$$

$$\beta = 1 + \frac{c-\sqrt{c^2+4c}}{2}. \tag{S.17}$$

We can rearrange (S.15) into

$$c = \alpha + \frac{1}{\alpha} - 2. \tag{S.18}$$

Finally, plugging (S.18) into (S.14), (S.16), and (S.17) allows us to express G_k as a function of α

$$G_k = \left(\frac{\alpha^k + \alpha^{1-k}}{\alpha + 1} \right). \tag{S.19}$$

3 Defining region of interest in microfluidic experiments

3.1 Region of interest for long-term microfluidic experiments

During the long-term microfluidic experiments (§2.2), we monitored the cell confluency across a region where wall shear stress is homogeneous. We performed a CFD simulation to obtain the wall shear stress field across the entire bottom surface as given in Figure S5. We determined a region of interest (ROI) for the confluency measurement, where the wall shear stress at the bottom surface is 3 mPa.

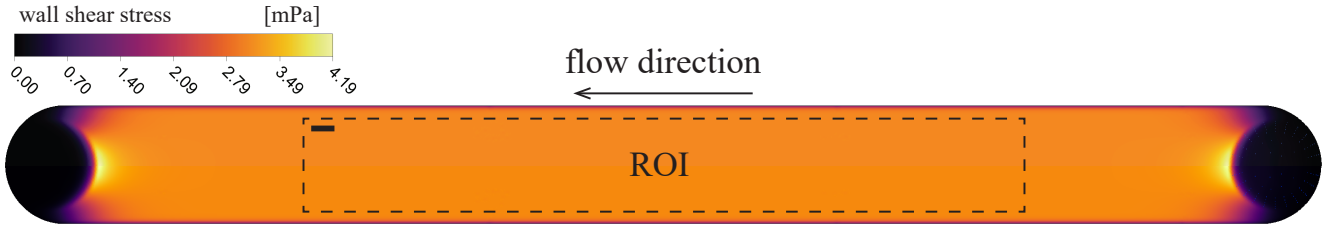

Figure S5. Region of interest for monitoring the cell confluency of static and flow cultures over 48 hours (§2.2). In the region (30 mm by 4 mm) centered at the channel, we have homogeneous wall shear stress of 3 mPa. Scale bar is 1 mm.

3.2 Region of interest for forced detachment experiments

For the forced detachment experiments (§2.3), we monitored the cell confluency across a region which was sufficiently upstream but still exhibited the wall shear stress of 30 mPa. This allowed us to minimize error in estimating confluency, that could be induced by the accumulation of astrocytes transferred from the upstream.

4 Confluency quantification

A Fiji/ImageJ plug-in based on a segmentation method proposed by Jaccard et al. [7] was used to estimate confluency of astrocytes. The algorithm performs segmentation using a local thresholding method supplemented by halo correction. The parameters of the algorithm are the standard deviation σ of a Gaussian kernel that is used to create the local contrast field of an image and local-contrast threshold ε. The parameters were set ($\sigma = 1.2$, $\varepsilon = 0.08$) to capture consistently astrocytes in phase-contrast images throughout this study. Figure S7 shows an example of the entire segmentation process. A phase-contrast image is processed by the segmentation algorithm first and is then de-speckled by a median filter whose radius was two pixels (2.64 μm). From the final image, we obtain the cell confluency.

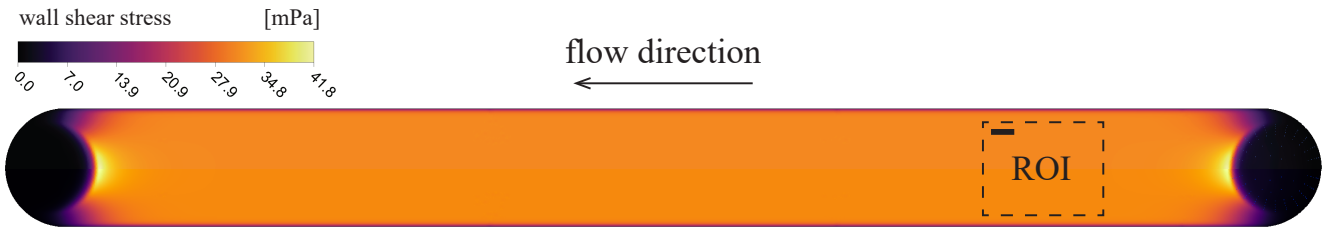

Figure S6. Region of interest (5 mm by 4 mm) for monitoring cell confluency in forced detachment experiments §2.3. The region to the right of the ROI was not optically measurable due to tubing connected to the inlet, letting us define the region of interest (ROI) as shown here. Scale bar is 1 mm.

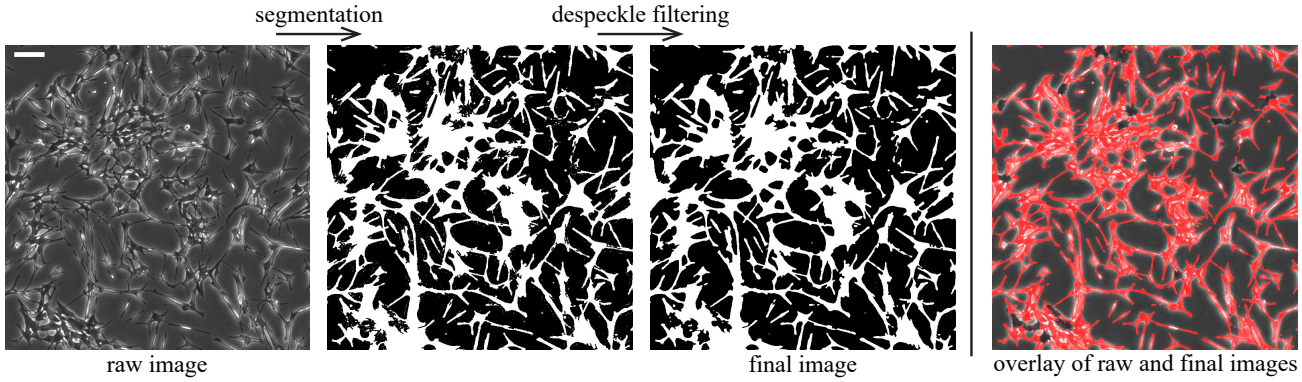

Figure S7. Image segmentation used in astrocyte confluency estimation. Binarization based on a local contrast thresholding method is performed, followed by noise reduction using median filter. The image is from a static culture at T = 72 h, whose seeding density was 2.0×10^4 cells/cm^2. Scale bar is 1 mm.

5 Dependence on dimensionless numbers

As given in the main article, the PNM provides the MWSS levels at the k^{th} hole and lumen as follows

$$\tau_k^{\mathscr{H}} = \frac{G_k}{m\hat{d}^{\,3}\sum_{i=1}^{n} G_i}\tau_d, \tag{S.20}$$

$$\tau_k^{\mathscr{L}} = \frac{\sum_{i=1}^{k} G_i}{\sum_{i=1}^{n} G_i}\tau_d = F_k\tau_d. \tag{S.21}$$

In the above expressions, G_k is defined as

$$G_k = \left(\frac{\alpha^k + \alpha^{1-k}}{\alpha+1}\right), \tag{S.22}$$

where

$$\alpha = 1 + \frac{c+\sqrt{c^2+4c}}{2} \quad \text{and} \quad c = \frac{m\hat{d}^{\,4}}{\hat{l}}. \tag{S.23}$$

Here, using (S.20) and (S.21), we give mathematical proofs for the monotonic changes of the MWSS levels with respect to the dimensionless numbers.

5.1 Dependence of $\tau_1^{\mathscr{H}}$ to $\hat{l}$

In order to show that $\tau_1^{\mathscr{H}}$ is monotonically increasing with respect to $\hat{l}$, we show that $\frac{\partial \sum_{i=1}^{n} G_i}{\partial \hat{l}}$ is negative. From (8), the following equations hold:

$$\begin{aligned} G_1 &= \frac{1}{c}(G_2 - G_1), \\ G_1 + G_2 &= \frac{1}{c}(G_3 - G_2), \\ G_1 + G_2 + G_3 &= \frac{1}{c}(G_4 - G_3), \\ &\vdots \\ G_1 + G_2 + \cdots + G_{k-1} &= \frac{1}{c}(G_k - G_{k-1}) \ \text{ for } \ 2 \le k. \end{aligned} \tag{S.24}$$

Summing up all the above gives:

$$(k-1)G_1 + (k-2)G_2 + (k-3)G_3 + \cdots + 2G_{k-2} + G_{k-1} = \frac{1}{c}(G_k - G_1). \tag{S.25}$$

Differentiating (S.25) with respect to c, reads:

$$(k-1)\frac{dG_1}{dc} + (k-2)\frac{dG_2}{dc} + (k-3)\frac{dG_3}{dc} + \cdots + 2\frac{dG_{k-2}}{dc} + \frac{dG_{k-1}}{dc} = \frac{1}{c}(\frac{dG_k}{dc} - \frac{dG_1}{dc}) - \frac{1}{c^2}(G_k - G_1). \tag{S.26}$$

Rearranging (S.26), we obtain:

$$\frac{dG_k}{dc} = \frac{1}{c}(G_k - G_1) + c\Big((k-1)\frac{dG_1}{dc} + (k-2)\frac{dG_2}{dc} + (k-3)\frac{dG_3}{dc} + \cdots + 2\frac{dG_{k-2}}{dc} + \frac{dG_{k-1}}{dc}\Big) + \frac{dG_1}{dc}. \tag{S.27}$$

From (S.22),

$$G_1 = 1, \tag{S.28}$$

$$\frac{dG_1}{dc} = 0, \tag{S.29}$$

$$G_k - 1 > 0 \ \text{ for } \ 2 \le k. \tag{S.30}$$

From (S.27) – (S.30), if $\frac{dG_i}{dc} > 0$ for $2 \le i \le (k-1)$, then $\frac{dG_k}{dc} > 0$.

Equation (S.22) gives $\frac{dG_2}{dc}$:

$$\frac{dG_2}{dc} = \frac{d}{dc}(c+1) = 1 > 0. \tag{S.31}$$

Using mathematical induction on (S.27) – (S.31):

$$\frac{dG_k}{dc} > 0 \ \text{ for } \ 2 \le k. \tag{S.32}$$

Equation (S.32) can further extend to

$$\sum_{i=1}^{n} \frac{dG_i}{dc} = \frac{d}{dc}\sum_{i=1}^{n} G_i > 0 \ \text{ for } \ 2 \le n. \tag{S.33}$$

The derivative of $\sum_{i=1}^{n} G_i$ with respect to $\hat{l}$ is

$$\frac{\partial}{\partial \hat{l}}\sum_{i=1}^{n} G_i = \frac{\partial}{\partial \hat{l}}\sum_{i=1}^{n} G_i = \frac{\partial c}{\partial \hat{l}}\frac{d}{dc}\sum_{i=1}^{n} G_i, \tag{S.34}$$

which should be negative, given that inequality (S.33) is true and $\frac{\partial c}{\partial \hat{l}} < 0$ from (S.23).

5.2 Dependence of $\tau_k^{\mathscr{L}}$ to $\hat{l}$

Here, we show that $\tau_k^{\mathscr{L}}$ is monotonically increasing with $\hat{l}$. Given $\tau_k^{\mathscr{L}} = F_k \tau_d$, this requires us to show that

$$\frac{\partial F_k}{\partial \hat{l}} = \frac{\partial}{\partial \hat{l}} \left(\frac{\sum_{i=1}^{k} G_i}{\sum_{i=1}^{n} G_i} \right) > 0 \quad \text{for} \quad 1 \leq k \leq (n-1). \tag{S.35}$$

From chain rule, the above becomes

$$\frac{\partial}{\partial \hat{l}} \left(\frac{\sum_{i=1}^{k} G_i}{\sum_{i=1}^{n} G_i} \right) = \frac{\partial c}{\partial \hat{l}} \frac{d}{dc} \left(\frac{\sum_{i=1}^{k} G_i}{\sum_{i=1}^{n} G_i} \right) > 0 \quad \text{for} \quad 1 \leq k \leq (n-1). \tag{S.36}$$

Given that $\frac{\partial c}{\partial \hat{l}}$ is negative from (S.23), the above inequality is equivalent to

$$\frac{d}{dc} \left(\frac{\sum_{i=1}^{k} G_i}{\sum_{i=1}^{n} G_i} \right) < 0 \quad \text{for} \quad 1 \leq k \leq (n-1). \tag{S.37}$$

We now show that the inequality (S.37) is true. From equation (S.24),

$$\frac{\sum_{i=1}^{k} G_i}{\sum_{i=1}^{n} G_i} = \frac{G_{k+1} - G_k}{G_{n+1} - G_n}. \tag{S.38}$$

Substituting (S.22) into (S.38), we obtain

$$\frac{G_{k+1} - G_k}{G_{n+1} - G_n} = \frac{\alpha^k - \alpha^{-k}}{\alpha^n - \alpha^{-n}}, \quad \text{where} \quad \alpha = 1 + \frac{c + \sqrt{c^2 + 4c}}{2}. \tag{S.39}$$

Based on the above,

$$\begin{aligned} \frac{d}{dc} \left(\frac{\sum_{i=1}^{k} G_i}{\sum_{i=1}^{n} G_i} \right) &= \frac{d}{dc} \left(\frac{G_{k+1} - G_k}{G_{n+1} - G_n} \right) = \frac{d}{dc} \left(\frac{\alpha^k - \alpha^{-k}}{\alpha^n - \alpha^{-n}} \right) \\ &= \underbrace{-\frac{d\alpha}{dc} \frac{\alpha^{-k+n-1}}{(\alpha^n - 1)^2 (\alpha^n + 1)^2}}_{f(\alpha)} \underbrace{(-k\alpha^{2k+2n} + n\alpha^{2k+2n} + n\alpha^{2k} - k\alpha^{2n} + k\alpha^{2k} - n\alpha^{2n} + k - n)}_{g(\alpha)}. \end{aligned} \tag{S.40}$$

Given the definition of α in (S.39), $f(\alpha)$ is always negative. Therefore, the above derivative is negative if and only if $g(\alpha)$ is positive. This allows us to restate the claim to be shown as follows:

$$g(1) = 0, \tag{S.41}$$

$$\frac{d\big(g(\alpha)\big)}{dc} = \frac{d\alpha}{dc} \frac{d\big(g(\alpha)\big)}{d\alpha} > 0, \quad \text{when} \quad \alpha > 1. \tag{S.42}$$

Showing the validity of (S.41) is trivial. For the inequality (S.42) consider first that $\frac{d\alpha}{dc}$ is positive according to the definition of α, so we have to show that $\frac{d(g(\alpha))}{d\alpha} > 0$. After algebraic manipulation, we obtain

$$\frac{d\big(g(\alpha)\big)}{d\alpha} > 0 \quad \text{if and only if} \quad \frac{b^n - b^{n-k}}{b^n - 1} > \frac{k}{n}, \quad \text{where} \quad b = \alpha^2. \tag{S.43}$$

We start by showing that $\frac{b^n - b^{n-k}}{b^n - 1} > \frac{k}{n}$ when $k = n-1$, to be used with induction to elucidate that the inequality holds also for all k less than n.

When $k = n-1$,

$$\frac{b^n - b^{n-(n-1)}}{b^n - 1} > \frac{n-1}{n}. \tag{S.44}$$

Rearranging the above inequality,

$$(b-1)(b^{n-1} + b^{n-2} + \cdots + b + 1 - n) > 0, \tag{S.45}$$

which holds for all n given that $b > 1$.
Now, assuming that

$$\frac{b^n - b^{n-k}}{b^n - 1} > \frac{k}{n}, \tag{S.46}$$

we aim to show that

$$\frac{b^n - b^{n-(k-1)}}{b^n - 1} > \frac{k-1}{n}. \tag{S.47}$$

Using inequality (S.46),

$$\frac{b^n - b^{n-(k-1)}}{b^n - 1} = \left(\frac{b^n - b^{n-k}}{b^n - 1}\right)\left(\frac{b^n - b^{n-(k-1)}}{b^n - b^{n-k}}\right) > \frac{k}{n}\left(\frac{b^n - b^{n-(k-1)}}{b^n - b^{n-k}}\right), \tag{S.48}$$

we now want to show that

$$\frac{k}{n}\left(\frac{b^n - b^{n-(k-1)}}{b^n - b^{n-k}}\right) > \frac{k-1}{n}. \tag{S.49}$$

Using equality $(b^n - 1) = (b-1)(b^{n-1} + b^{n-2} + \cdots + b + 1)$, we can rearrange inequality (S.49) as follows

$$b^{k-1} + b^{k-2} + \cdots + b^2 + b > k - 1. \tag{S.50}$$

For $b > 1$, the above equality holds for every k. By the principle of mathematical induction, the claim (S.42) is thus proved and we showed that $\tau_k^{\mathscr{L}}$ monotonically increases with $\hat{l}$.

5.3 Dependence of $\tau_k^{\mathscr{H}}$ to $\hat{d}$

Here, we aim to prove that

$$\frac{\partial \tau_k^{\mathscr{H}}}{\partial \hat{d}} = \frac{\partial}{\partial \hat{d}}\left(\frac{G_k}{m\hat{d}^{\,3}\sum_{i=1}^n G_i}\tau_d\right) = \frac{\tau_d}{m}\frac{\partial}{\partial \hat{d}}\left(\frac{G_k}{\hat{d}^{\,3}\sum_{i=1}^n G_i}\right) < 0. \tag{S.51}$$

Since $\tau_d/m > 0$, proving the above inequality is equivalent to showing that

$$\begin{aligned}\frac{\partial}{\partial \hat{d}}\left(\frac{G_k}{\hat{d}^{\,3}\sum_{i=1}^n G_i}\right) &= \frac{\partial}{\partial \hat{d}}\left(\frac{G_n}{\hat{d}^{\,3}\sum_{i=1}^n G_i}\frac{G_k}{G_n}\right) \\ &= \underbrace{\frac{\partial}{\partial \hat{d}}\left(\frac{G_n}{\hat{d}^{\,3}\sum_{i=1}^n G_i}\right)}_{h(\hat{d})}\frac{G_k}{G_n} + \underbrace{\frac{\partial}{\partial \hat{d}}\left(\frac{G_k}{G_n}\right)}_{p(\hat{d})}\frac{G_n}{\hat{d}^{\,3}\sum_{i=1}^n G_i} < 0.\end{aligned} \tag{S.52}$$

Both $\frac{G_k}{G_n}$ and $\frac{G_n}{\hat{d}^{\,3}\sum_{i=1}^n G_i}$ are positive, leading us to claim that both $h(\hat{d})$ and $p(\hat{d})$ are negative.
Let's show first that

$$h(\hat{d}) = \frac{\partial}{\partial \hat{d}}\left(\frac{G_n}{\hat{d}^{\,3}\sum_{i=1}^n G_i}\right) < 0. \tag{S.53}$$

From the definition of α and G_k, we have

$$\frac{1}{\hat{d}^{\,3}} = \left(\frac{m\alpha}{\hat{l}(\alpha-1)^2}\right)^{3/4}, \tag{S.54}$$

$$\frac{G_k}{\sum_{i=1}^n G_i} = \frac{(\alpha-1)(\alpha+\alpha^{2k})\alpha^{-1-k+n}}{\alpha^{2n}-1}. \tag{S.55}$$

Plugging (S.54) and (S.55) into equation (S.53), we have

$$\frac{\partial \alpha}{\partial \hat{d}}\left(\frac{3\alpha - \alpha^2 + \alpha^{4n} - 3\alpha^{4n+1} + \alpha^{2n+2}(1-8n) + \alpha^{2n}(-1+8n)}{4\alpha^2(\alpha+\alpha^{-1}-2)^{3/4}(\alpha^{2n}-1)^2}\right) < 0. \tag{S.56}$$

Since both $\partial\alpha/\partial\hat{d}$ and $4\alpha^2(\alpha+\alpha^{-1}-2)^{3/4}(\alpha^{2n}-1)^2$ are positive, inequality (S.56) is equivalent to

$$3\alpha-\alpha^2+\alpha^{4n}-3\alpha^{4n+1}+\alpha^{2n+2}(1-8n)+\alpha^{2n}(-1+8n)=q(\alpha)<0. \tag{S.57}$$

$q(\alpha)$ can be rearranged into

$$\begin{aligned} q(\alpha) &= 3\alpha-\alpha^2+\alpha^{4n}-3\alpha^{4n+1}+\alpha^{2n+2}(1-8n)+\alpha^{2n}(-1+8n) \\ &= -(\alpha-1)\big(2(\alpha^{4n-1}+\alpha^{4n-2}+\cdots+\alpha^3+\alpha^2)+3(\alpha^{4n}+\alpha)+(8n-1)\alpha^{2n}(\alpha+1)\big), \end{aligned} \tag{S.58}$$

which is negative, given $\alpha>1$ and $n>1$. This therefore proves that $h(\hat{d})<0$.

Now, let's show that

$$p(\hat{d})=\frac{\partial}{\partial\hat{d}}\left(\frac{G_k}{G_n}\right)<0. \tag{S.59}$$

Using the definition of G_k,

$$\begin{aligned} p(\hat{d})=\frac{\partial}{\partial\hat{d}}\left(\frac{G_k}{G_n}\right)=\frac{\partial}{\partial\hat{d}}\left(\frac{\alpha^{1-k}+\alpha^k}{\alpha^{1-n}+\alpha^n}\right)=\frac{\partial\alpha}{\partial\hat{d}}\frac{d}{d\alpha}\left(\frac{\alpha^{1-k}+\alpha^k}{\alpha^{1-n}+\alpha^n}\right) \\ =\frac{\partial\alpha}{\partial\hat{d}}\left(\frac{\alpha^{n-k-1}\big((n-k)(\alpha^2-\alpha^{2(n+k)})+(n+k-1)\alpha^{2k+1}(1-\alpha^{2(n-k)})\big)}{(\alpha+\alpha^{2n})^2}\right). \end{aligned} \tag{S.60}$$

Provided that $n>k>0$, $\alpha>1$, and $\frac{\partial\alpha}{\partial\hat{d}}>0$, $p(\hat{d})$ is negative by (S.60) .

We showed that both $h(\hat{d})$ and $p(\hat{d})$ are negative, proving the claim inequality (S.51).

5.4 Dependence of $\tau_k^{\mathscr{H}}$ to m

Here, we want to prove that

$$\frac{\partial\tau_k^{\mathscr{H}}}{\partial m}=\frac{\partial}{\partial m}\left(\frac{G_k}{m\hat{d}^{\,3}\sum_{i=1}^n G_i}\tau_d\right)=\frac{\tau_d}{\hat{d}^{\,3}}\frac{\partial}{\partial m}\left(\frac{G_k}{m\sum_{i=1}^n G_i}\right)<0. \tag{S.61}$$

Since $\tau_d/\hat{d}^{\,3}>0$, proving the above expression is equivalent to

$$\begin{aligned} \frac{\partial}{\partial m}\left(\frac{G_k}{m\sum_{i=1}^n G_i}\right)=\frac{\partial}{\partial m}\left(\frac{G_n}{m\sum_{i=1}^n G_i}\frac{G_k}{G_n}\right) \\ =\underbrace{\frac{\partial}{\partial m}\left(\frac{G_n}{m\sum_{i=1}^n G_i}\right)}_{q(m)}\frac{G_k}{G_n}+\underbrace{\frac{\partial}{\partial m}\left(\frac{G_k}{G_n}\right)}_{r(m)}\frac{G_n}{m\sum_{i=1}^n G_i}<0. \end{aligned} \tag{S.62}$$

Both $\frac{G_k}{G_n}$ and $\frac{G_n}{m\sum_{i=1}^n G_i}$ are positive, leading us to claim that both $q(m)$ and $r(m)$ are negative.

Let's show first that

$$q(m)=\frac{\partial}{\partial m}\left(\frac{G_n}{m\sum_{i=1}^n G_i}\right)<0. \tag{S.63}$$

From the definition of α and G_k, we have

$$\frac{1}{m}=\frac{\hat{d}^{\,4}}{\hat{l}}\left(\frac{\alpha}{(\alpha-1)^2}\right), \tag{S.64}$$

$$\frac{G_k}{\sum_{i=1}^n G_i}=\frac{(\alpha-1)(\alpha+\alpha^{2k})\alpha^{-1-k+n}}{\alpha^{2n}-1}. \tag{S.65}$$

Inserting (S.64) and (S.65) into (S.63), we have

$$\frac{\partial\alpha}{\partial m}\left(\frac{\alpha-\alpha^{4n+1}+2n\alpha^{2n}-2n\alpha^{2n+2}}{(\alpha-1)^2\alpha(\alpha^n-1)^2(\alpha^n+1)^2}\right)<0. \tag{S.66}$$

Since both $\partial\alpha/\partial m$ and $(\alpha-1)^2\alpha(\alpha^n-1)^2(\alpha^n+1)^2$ are positive, inequality (S.66) is equivalent to

$$\alpha-\alpha^{4n+1}+2n\alpha^{2n}-2n\alpha^{2n+2}=w(\alpha)<0. \tag{S.67}$$

$w(\alpha)$ can be rearranged into

$$w(\alpha)=\alpha(1-\alpha^{4n})+2n\alpha^{2n}(1-\alpha^2), \tag{S.68}$$

which should be less than zero, given $\alpha>1$ and $n>1$. This therefore proves $q(m)<0$.

Now, let's show that

$$r(m)=\frac{\partial}{\partial m}\left(\frac{G_k}{G_n}\right)<0. \tag{S.69}$$

Using the definition of G_k,

$$r(m)=\frac{\partial}{\partial m}\left(\frac{\alpha^{1-k}+\alpha^k}{\alpha^{1-n}+\alpha^n}\right)=\frac{\partial\alpha}{\partial m}\frac{d}{d\alpha}\left(\frac{\alpha^{1-k}+\alpha^k}{\alpha^{1-n}+\alpha^n}\right). \tag{S.70}$$

We show that $\frac{d}{d\alpha}\left(\frac{\alpha^{1-k}+\alpha^k}{\alpha^{1-n}+\alpha^n}\right)<0$ in (S.60). Provided that $n>k>0$, $\alpha>1$, and $\frac{\partial\alpha}{\partial m}>0$, $r(m)$ should be less than zero.

We showed that both $q(m)$ and $r(m)$ are negative, thus proving the claim inequality (S.61).

5.5 Dependence of $\tau_k^{\mathscr{L}}$ to $\hat{d}$ and to m

Since both $\frac{\partial c}{\partial\hat{d}}$ and $\frac{\partial c}{\partial\hat{m}}$ are positive by (S.23), proving $\frac{\partial\tau_k^{\mathscr{L}}}{\partial c}<0$ is sufficient to show that

$$\frac{\partial\tau_k^{\mathscr{L}}}{\partial\hat{d}}<0 \quad\text{and}\quad \frac{\partial\tau_k^{\mathscr{L}}}{\partial m}<0. \tag{S.71}$$

By the definition of $\tau_k^{\mathscr{L}}$, we have

$$\frac{\partial\tau_k^{\mathscr{L}}}{\partial c}=\frac{\partial}{\partial c}\left(\frac{\sum_{i=1}^k G_i}{\sum_{i=1}^n G_i}\tau_d\right)=\tau_d\frac{d}{dc}\left(\frac{\sum_{i=1}^k G_i}{\sum_{i=1}^n G_i}\right)<0, \tag{S.72}$$

which is true since inequality (S.37) holds.

5.6 Graphical representation of effects of dimensionless numbers

While the prior section offers the mathematical proofs of the monotonic changes of the MWSS values with respect to dimensionless numbers, here, we additionally provide graphical representations (Fig. S8) that show such monotonic changes of MWSS values over changing dimensionless numbers. All graphs here result from the PNM.

6 Viscosity measurement of human subject CSF

The CSF collection from 37 patients was approved by the Institutional Review Board at Boston Medical Center (BMC; approval number H-37724), and informed consent was obtained from each participant prior to collection of non-infectious CSF from patients undergoing Lumbar Puncture (LP) at BMC's neurology clinic. The samples were from patients with pseudotumor (n = 26), papilledema (n = 6), headaches (n = 2), multiple sclerosis (n = 1), gait instability (n = 1), and neurosyphilis (n = 1) (Tab. 1).

The collected samples were preserved at $-80^{\cdot}$C before commencing with the viscosity measurement using a rotational shear rheometer with a 60 mm cone head (Discovery HR-1, TA Instruments). The viscosity was measured under *shear rates* $\dot{\gamma}$ that ranges from 85 to 1,000 s^{-1}; at shear rates under 85 s^{-1}, we found that an error due to surface tension occurring at the interface between the head and sample became important [6], as is expected for these low ranges of viscosity close to water. This can be seen in Figures S9 and S10, where the viscosity of CSF (at 37$^{\cdot}$C) is shown to be larger than that of water (0.69 mPa·s), exhibiting slight shear thinning particularly under ~500 s^-1.

CSF index	diagnosis	CSF index	diagnosis	CSF index	diagnosis	CSF index	diagnosis
1	pseudotumor	11	pseudotumor	21	pseudotumor	31	pseudotumor
2	pseudotumor	12	pseudotumor	22	papilledema	32	pseudotumor
3	papilledema	13	pseudotumor	23	multiple sclerosis	33	pseudotumor
4	pseudotumor	14	pseudotumor	24	pseudotumor	34	pseudotumor
5	pseudotumor	15	papilledema	25	pseudotumor	35	headaches
6	pseudotumor	16	pseudotumor	26	gait instability	36	pseudotumor
7	pseudotumor	17	pseudotumor	27	papilledema	37	headaches
8	pseudotumor	18	papilledema	28	pseudotumor		
9	pseudotumor	19	pseudotumor	29	pseudotumor		
10	pseudotumor	20	pseudotumor	30	neurosyphilis		

Table 1. Diagnoses of 37 CSF samples. The index used here is matched with that of Figures S9 – S12. No hemorrhage was involved in all samples.

6.1 Characterization of shear thinning

We use the the Ostwald–de Waele power-law [12], which has been widely used to describe non-newtonian fluids [1; 4]. Considering a circular pipe flow described in cylindrical coordinate system. The shear stress, τ, of an Ostwald–de Waele fluid follows

$$\tau = K\left(-\frac{\partial u_z}{\partial r}\right)^n = \underbrace{-K\left[\left(-\frac{\partial u_z}{\partial r}\right)^{n-1}\right]}_{\mu}\left(\frac{\partial u_z}{\partial r}\right), \tag{S.73}$$

where K is the flow consistency index (Pa $\cdot$ s^n), $\frac{\partial u_z}{\partial r}$ is the shear rate (s^{-1}), n is the dimensionless flow behavior number, and μ is the viscosity of the fluid (Pa $\cdot$ s).

In the law, $n > 1$, $n < 1$, and $n = 1$ represent shear thickening, thinning, and Newtonian behavior, respectively. We estimate the flow behavior index n of each CSF human subject sample, using curve-fitting over $\dot{\gamma} = 85 - 300$ s^{-1}, where shear thinning is clearly observed. The flow behavior indices of all of the CSF samples lie in the 0.71 – 0.95 range, with mean value of 0.83 and standard deviation of 0.06.

Here, we show that the Poiseuille assumption provides us a conservative estimate of wall shear stress in the catheter system, *i.e.*, lower WSS than that estimated from the power-law (S.73). Indeed, the power-law, (S.73), provides the wall shear stress of the fully-developed laminar flow in a circular tube as

$$\tau_w = K\left[\left(\frac{3n+1}{n}\right)\frac{8Q}{\pi D^3}\right]^n, \tag{S.74}$$

where Q is the flow rate, and D is the diameter of the tube. To quantify the order of magnitude of the ratio between WSS levels under a Newtonian and a shear thinning assumption we make the comparison at the lumen's most downstream point of the catheter (*e.g.*, L8 in Figure 10). Matching the total flow rate, we introduce the ratio between the WSS levels defined by (S.74) and the Poiseuille's law.

$$r = \frac{\tau_w|_{\text{power-law}}}{\tau_w|_{\text{Poiseuille}}} = \frac{K}{4\mu}\left(\frac{3n+1}{n}\right)^n\left(\frac{8Q}{\pi D^3}\right)^{n-1}. \tag{S.75}$$

To estimate this ratio, we use the sets of K and n that can be obtained from the measured data (Figs. S9 – S12). In current commercial shunt, the upper bound of the flow rate is 1 mL/min and the lower bound of D is 1 mm [5; 11]. Setting $\mu = 0.8$ mPa, which is close to the smallest viscosity that the samples have (Figs. S9 – S12), we obtain a lower bound of the ratio $3.83 < r < 6.33$. Hence, Poiseuille's law with $\mu = 0.8$ mPa provides a conservative value of WSS – lower than that of the power-law – when optimizing catheter design to maximize shear stress.

Note that the above analysis provides us first-order estimates, given the inherent limitation of the power-law: its non-physical predictions of zero viscosity as $\partial u_z/\partial r \to \infty$ or infinite viscosity at zero shear rate; yet, realistic fluids would have maximum and minimum viscosity values that are inherent to the physico-chemistry of the fluid. The law can provide a reasonable estimate of viscosity over the range of shear rates across which the curve-fitting is performed, but not necessarily for the other ranges. Our CFD simulations of the catheter flow, with Newtonian CSF, provide an order of magnitude of the upper bound of the shear rate involved: ~ 300 s^{-1}. Our curve-fitting for the power law is performed for $\dot{\gamma} = 85$ - 300 s^{-1}.

In order to have more accurate estimation for the ratio (S.75), we further performed CFD simulations (Fluent 2019 R1), considering shear thinning described by the power-law (S.73) with the upper and lower bounds of shear rate where the law is valid. In the simulations, we used the scenario 1's catheter in §4.2, finding that WSS under the Newtonian condition is indeed smaller than those under the power-law conditions (Fig. S13). Based on K and n from a sample (CSF15 in Figure S10), which shows the largest n among our samples, we design three different scenarios: 1) Newtonian CSF with μ = 0.8 mPa·s, which is the lowest viscosity of the sample; 2) shear thinning CSF that follows (S.73) for $\dot{\gamma}$ = 100 – 800 s^{-1}; and 3) shear thinning CSF that follows (S.73) for $\dot{\gamma}$ = 0.01 – 800 s^{-1}. The Reynolds number of the Newtonian scenario is 10, a moderate value of the regimes of the system, and all scenarios share the same flow rate. Note that both shear-thinning cases also have the lowest viscosity of 0.8 mPa·s. Given that the viscosity under $\dot{\gamma}$ = 85 s^{-1} was not measurable due to the capillary effect, we simulated two extreme cases, where the shear thinning disappears at 100 s^{-1}, slightly larger than the lower limit of the measurable range, or at 0.01 s^{-1}, a thousand times lower than for the first case. In either cases, we confirm that the MWSS at each section is larger than that estimated with the Newtonian fluid. Here, we can confirm that the Newtonian approximation provides the conservative limit to use for optimization of the catheter flow.

6.2 Inertia- and surface tension-induced bias in viscosity measurement

Measurement of low viscosity values of fluids using a rotational rheometer involves two major sources of error: inertia- and surface tension-induced errors [6]. The inertia error refers to an additional viscous dissipation due to secondary flow in the sample not sufficiently damped in low-viscosity fluids, or high Reynolds number regimes of operation in particular. In the measurement setting we have, the Reynolds number is defined as $Re_r = \frac{\rho\omega\beta^2R^2}{\mu}$, where ρ the sample density, μ is the sample dynamic viscosity, and ω, β, and R are the angular velocity, cone angle, and radius of the head, respectively. The additional torque on the head due to this inertia effect was calculated by Turian [13] to be

$$\frac{T}{T_o} = 1 + \frac{3}{4900}Re_r^2, \tag{S.76}$$

where T_o and T are the torque due to viscous dissipation without and with inertia effect, respectively. The measured viscosity is proportional to the measured torque [10]:

$$T = \frac{2\pi R^3\omega}{3\beta}\mu, \tag{S.77}$$

which applies to the viscosity measurement with a cone head. From (S.76) and (S.77), we obtain

$$\frac{\mu_m}{\mu_o} = 1 + \frac{3}{4900}\left(\frac{\rho\omega\beta^2R^2}{\mu_o}\right)^2, \tag{S.78}$$

where μ_m is the measured viscosity including inertia effect. In the above equation, we can solve for μ_o, the corrected viscosity. Note that all of the data given in Figures S9 – S12 are corrected by this method.

At low shear rates, an additional torque due to capillary effects on the head becomes important. Correcting for this effect is not trivial nor well understood [8]. Hence, we focus the range of shear rates for which the additional capillary-induced torque is negligible compare to the torque introduced by viscous forces.

We first performed viscosity measurement on deionized water, notoriously difficult due to the above two effects, at 37C· to find the lower bound of the range for water. Using the same protocols as those used for the CSF viscosity measurement, we measured the viscosity of water at 37·C and $\dot{\gamma}$ = 63 and 85 s^{-1} (n = 11). We performed one-pair t-tests on the data, having the null hypothesis that the viscosity of water is 0.69 mPa·s [9].

We found that the p-value of the data from $\dot{\gamma}$ = 8.5 s^{-1} is 0.03, while that from $\dot{\gamma}$ = 85 s^{-1} is 0.06. Applying a 5% significance level, we selected $\dot{\gamma}$ = 85 s^{-1} as the lower bound of the range for water where the surface tension effect can be neglected. The surface tension of CSF is lower than that of water at 37°C [2]. Moreover, the viscosity of CSF is higher than that of water as shown in our data. This concludes that the cutoff shear rate for CSF can be lower than that for water. Based on this, we select $\dot{\gamma}$ = 85 s^{-1} as cutoff shear rate for which measurement of viscosity of CSF is reasonably accurate.

7 Example of multi-objective optimization

We illustrate an example of the multi-objective optimization based on the Poiseuille network model (PNM) and a genetic algorithm [3]. This approach enables us to develop Pareto optimal solutions for which optimization of one design objective necessitates compromising another design objective. Using the gamultiobj function in MATLAB R2018b, we compute the

Pareto optimal solutions of catheters whose geometric structure is as shown in Figure 17a. Figure S14 shows a set of Pareto solutions with two design objective, namely 1) minimizing the standard deviation of flow rates across holes *and* 2) maximizing the minimum MWSS levels across all sections. Note that the PNM can be used to readily compute the flow rate distribution from the wall shear stress distribution, using Poiseuille's law (Eq. (S.6)).

8 Partial blockage and low wall shear stress zone formation

We offer a CFD simulation that illustrates how a partial blockage of one of the most proximal holes (*i.e.*, the highest hole index) of the catheter used in Scenario 1 in §4.2 can affect the wall shear stress distribution through the same hole. Figure S15 shows that a partial blockage at one of the most proximal hole induces strong inhomogeneity of the local wall shear stress distribution at the hole, resulting in the formation of zones where wall shear stress is less than that of the unblocked case. This result implies that upon partial blockage due, for example, bulk tissue aspiration the space between the aspirated tissue and the hole wall may favor cellular ingrowth that may in time lead to formation of adhesion between the bulk tissue and the locally adhering cells.

References

1. R. Bird, W. Stewart, and E. Lightfoot. *Transport Phenomena (revised second ed.)*. John Wiley & Sons, 2007.

2. H. Brydon, R. Hayward, W. Harkness, and R. Bayston. Physical properties of cerebrospinal fluid of relevance to shunt function. 2: The effect of protein upon CSF surface tension and contact angle. *British Journal of Neurosurgery*, 9(5): 645–652, 1995. doi: 10.1080/02688699550040936.

3. K. Deb. *Multi-objective optimization using evolutionary algorithms*, volume 16. John Wiley & Sons, 2001.

4. F. Delplace and J. Leuliet. Generalized Reynolds number for the flow of power law fluids in cylindrical ducts of arbitrary cross-section. *The Chemical Engineering Journal and The Biochemical Engineering Journal*, 56(2):33–37, 1995. doi: 10.1016/0923-0467(94)02849-6.

5. J. M. Drake and C. Sainte-Rose. *The shunt book*. Blackwell Science, 1995.

6. R. H. Ewoldt, M. T. Johnston, and L. M. Caretta. Experimental challenges of shear rheology: how to avoid bad data. In *Complex Fluids in Biological Systems*, pages 207–241. Springer, 2015. doi: 10.1007/978-1-4939-2065-5_6.

7. N. Jaccard, L. D. Griffin, A. Keser, R. J. Macown, A. Super, F. S. Veraitch, and N. Szita. Automated method for the rapid and precise estimation of adherent cell culture characteristics from phase contrast microscopy images. *Biotechnology and Bioengineering*, 111(3):504–517, 2014. doi: 10.1002/bit.25115.

8. M. T. Johnston and R. H. Ewoldt. Precision rheometry: Surface tension effects on low-torque measurements in rotational rheometers. *Journal of Rheology*, 57(6):1515–1532, 2013. doi: 10.1122/1.4819914.

9. J. Kestin, M. Sokolov, and W. A. Wakeham. Viscosity of liquid water in the range - 8 C to 150 C. *Journal of Physical and Chemical Reference Data*, 7(3):941–948, 1978. doi: 10.1063/1.555581.

10. H. Markovitz, L. Elyash, F. Padden Jr, and T. DeWitt. A cone-and-plate viscometer. *Journal of Colloid Science*, 10(2): 165–173, 1955. doi: 10.1016/0095-8522(55)90023-4.

11. Medtronic. *Neurosurgery product catalog*. 2016.

12. W. Ostwald. Ueber die Geschwindigkeitsfunktion der Viskosität disperser Systeme. I. *Colloid & Polymer Science*, 36(2): 99–117, 1925. doi: 10.1007/BF01431449.

13. R. M. Turian. Perturbation solution of the steady newtonian flow in the cone and plate and parallel plate systems. *Industrial & Engineering Chemistry Fundamentals*, 11(3):361–368, 1972. doi: 10.1021/i160043a014.

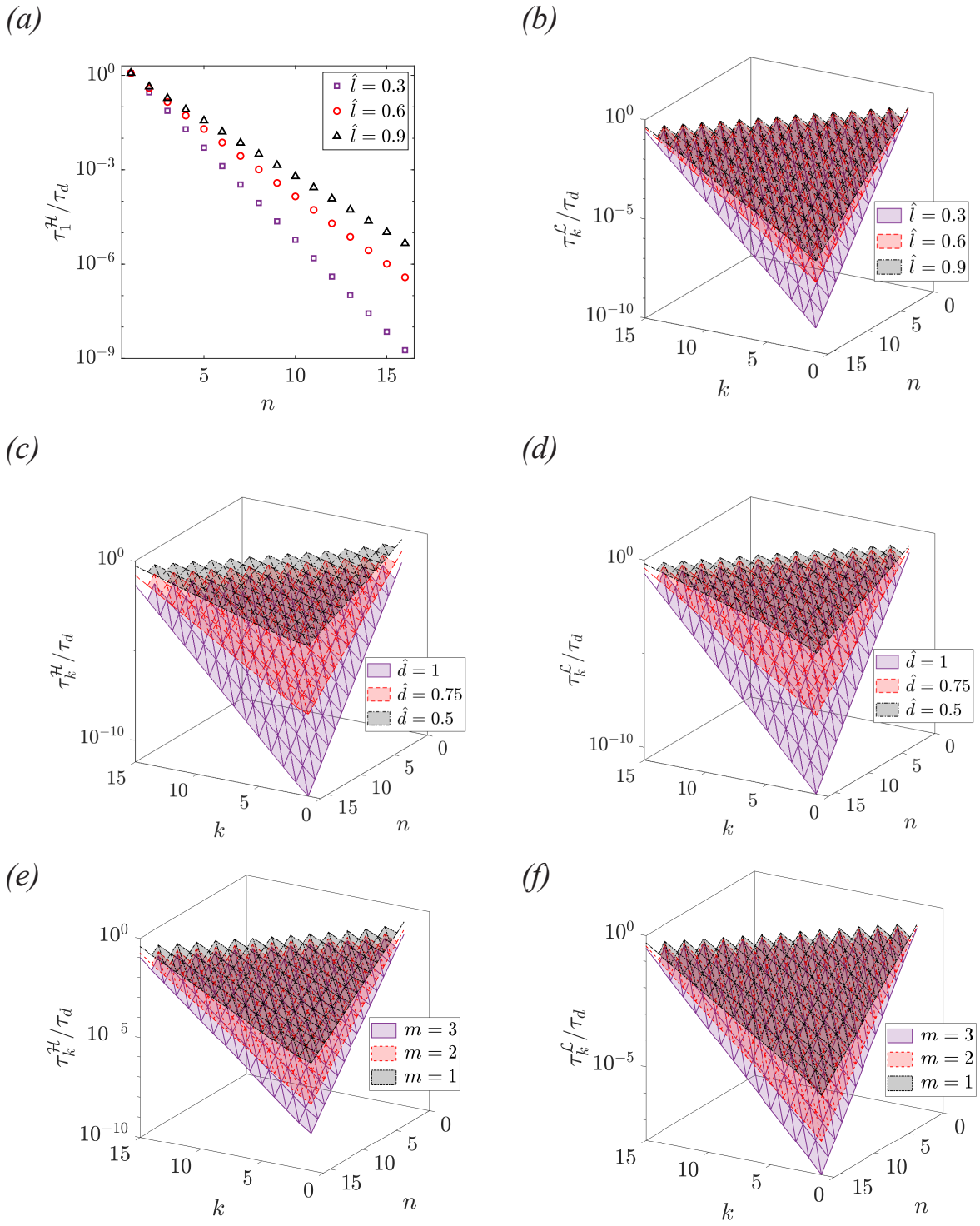

Figure S8. Monotonic changes of the MWSS levels with respect to different dimensionless numbers over different combinations of n and k. (a) the MWSS at the first hole (i.e., the minimum MWSS across holes) exhibits a monotonic increase with increased $\hat{l}$. (b) the MWSS levels at lumina also increase over increased $\hat{l}$. (c) and (d) the MWSS levels at holes and lumina increase with decreased $\hat{d}$. (e) and (f) the MWSS levels monotonically increase upon decreased m. In every graph, $m = 2$, $\hat{l} = 0.6$, and $\hat{d} = 0.75$, otherwise specified.

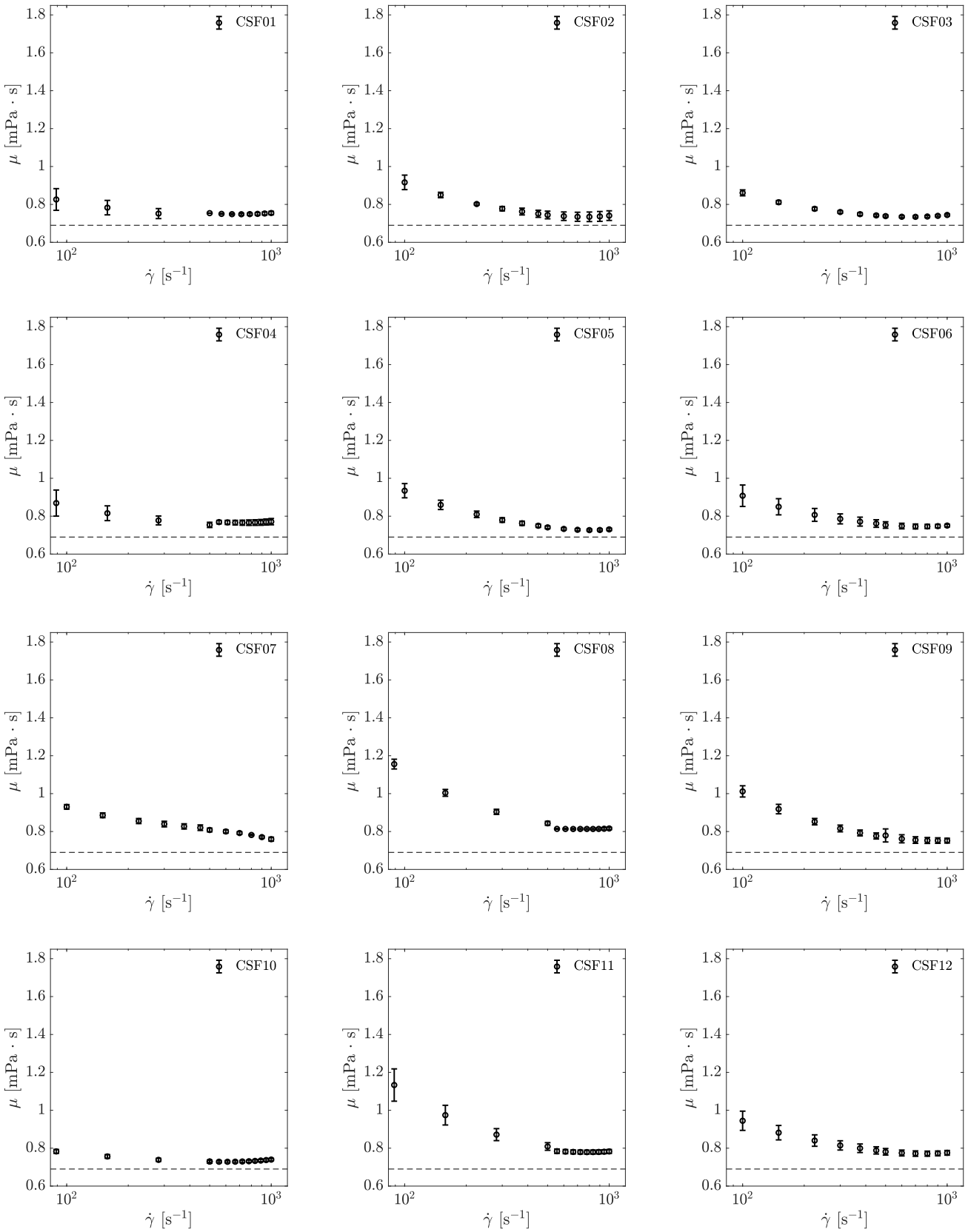

Figure S9. Viscosity of CSF samples (CSF01 – 12) from different patients. The dash line indicates the viscosity of water at 37°C. Error bars reflect the standard deviation over three independent measurement performed.

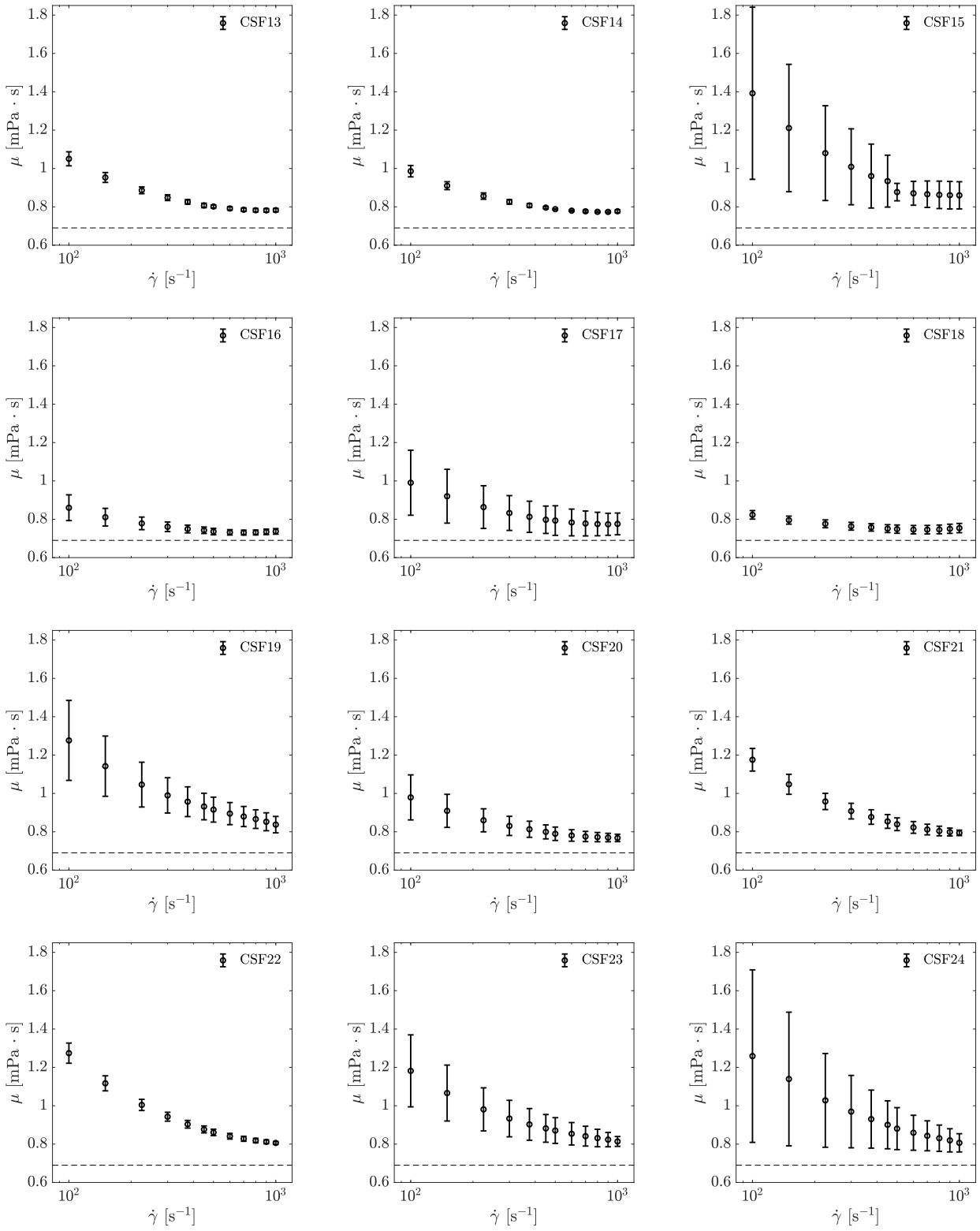

Figure S10. Viscosity of CSF samples (CSF13 – 24) from different patients. The dash line indicates the viscosity of water at 37°C. Error bars reflect the standard deviation over three independent measurement performed.

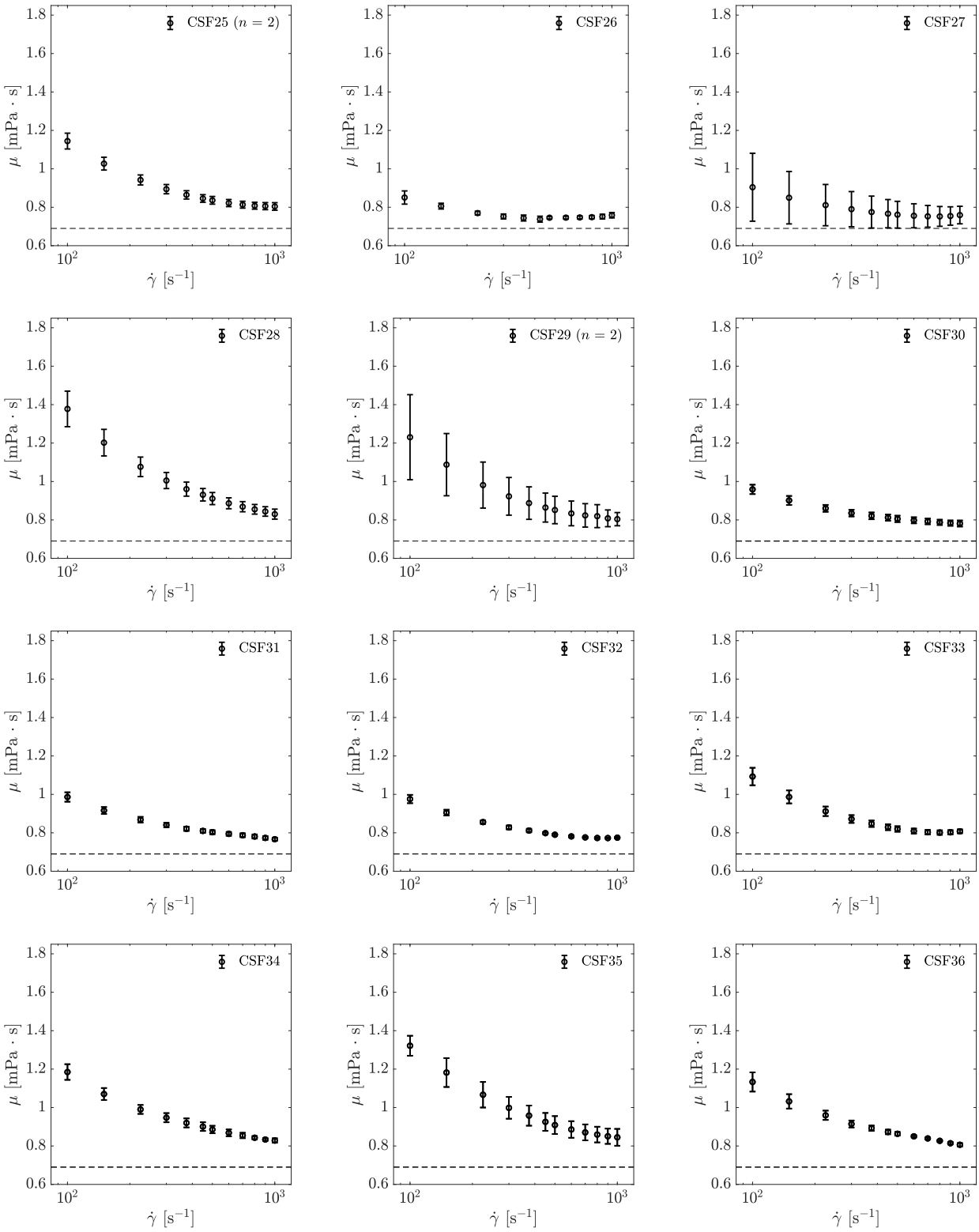

Figure S11. Viscosity of CSF samples (CSF25 – 36) from different patients. The dash line indicates the viscosity of water at 37°C. Error bars reflect the standard deviation over three independent measurement performed, except in CSF25 and 29 where two independent measurement performed.

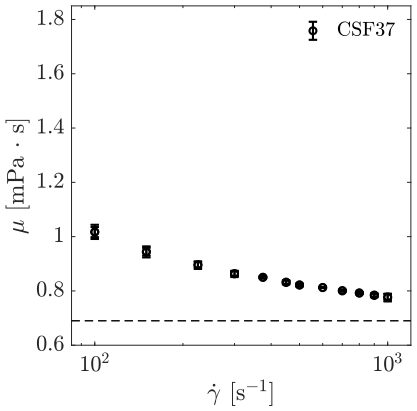

Figure S12. Viscosity of CSF sample (CSF37). The dash line indicates the viscosity of water at 37°C. Error bars reflect the standard deviation over three independent measurement performed.

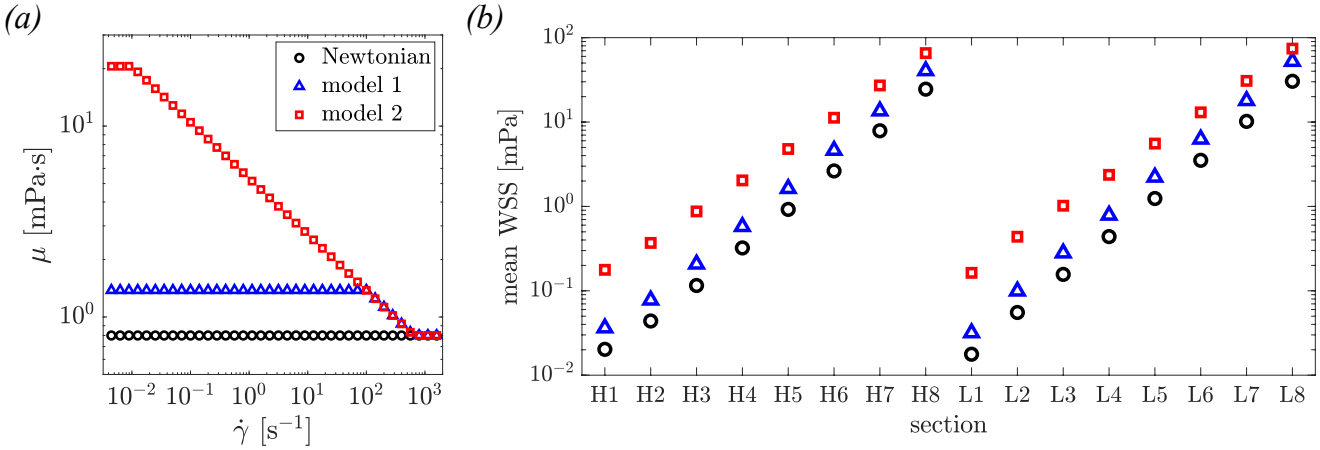

Figure S13. CFD simulations with the power-law describing shear thinning of CSF (S.73). (a) Two power-law models have different lower bounds for the range over which the (S.73) applies. K and n are 0.0053 and 0.71, respectively, sampled from CSF15 in Figure S10. Note that both models have the same lowest viscosity which is the viscosity of the Newtonian model. (b) Mean wall shear stress (MWSS) distribution calculated by CFD simulations with the viscosity models of (a). Shear thinning models give higher MWSS, compared to the Newtonian model. This confirms our first-order theoretical calculation for the ratio (S.75), given in §S-6.1

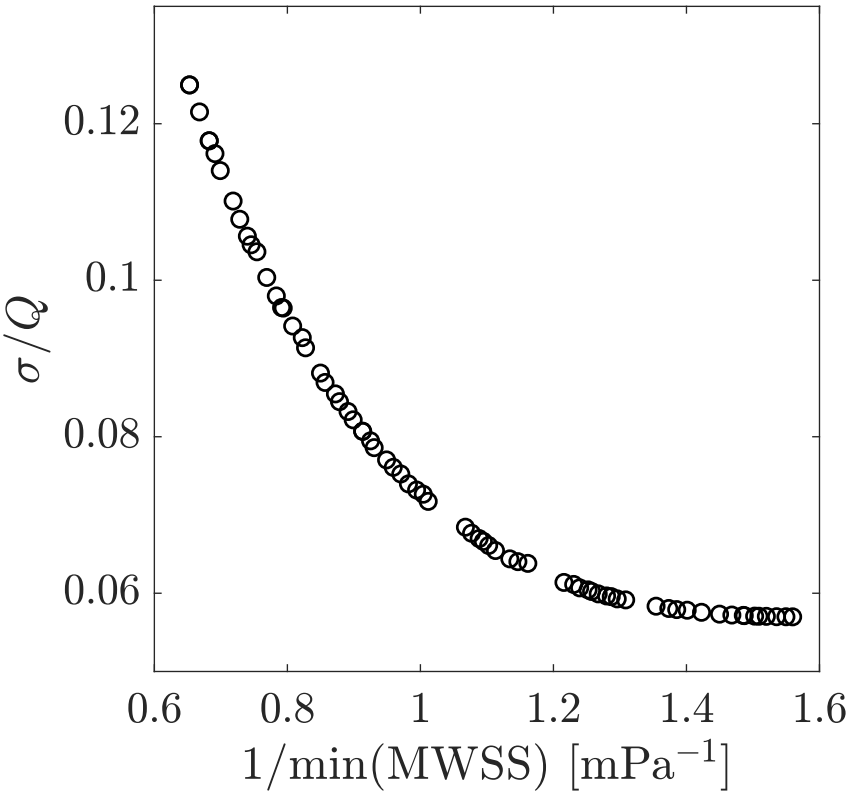

Figure S14. Pareto optimal solutions having two objectives: minimizing the standard deviation of flow rates and maximizing the minimum of MWSS values of sections. The y-axis is the standard deviation σ of flow rates, normalized by the total flow rate Q. The catheter geometry in Figure 17a is used under proper geometric constraints that are relevant and consistent with current commercial catheters. Note that the solution with the highest minimum MWSS (i.e., the most left-top) is indeed corresponding to the design in Figure 17b.

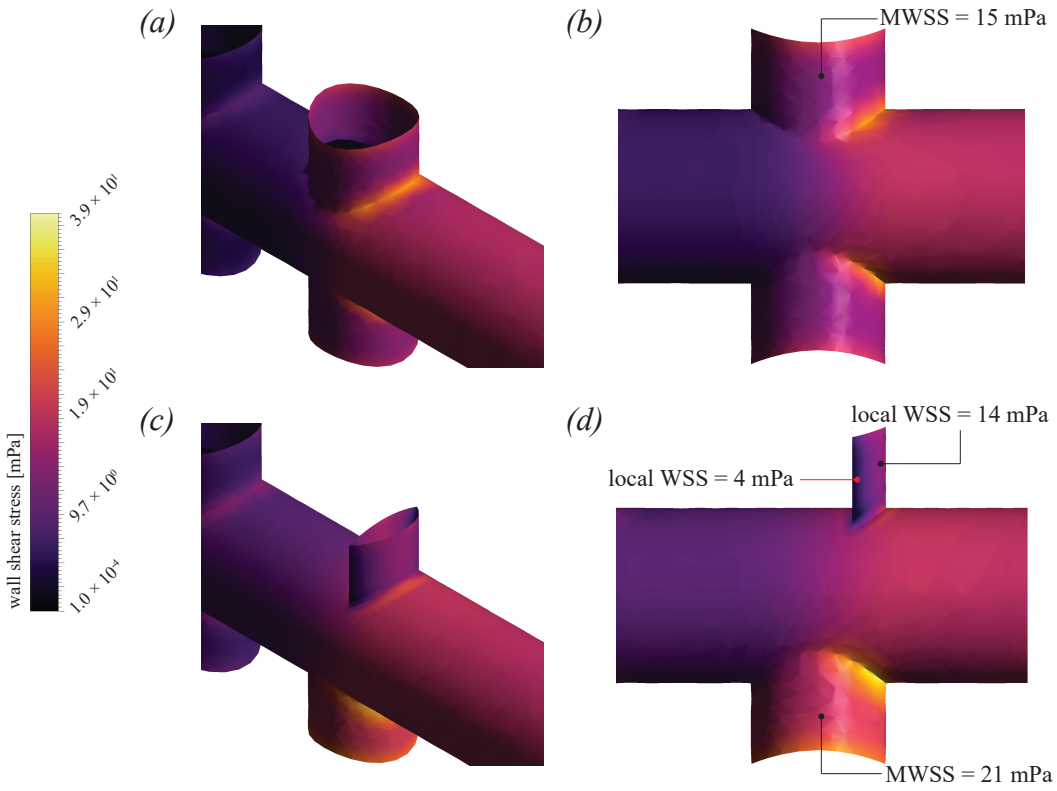

Figure S15. Effect of partial blockage of one of the most proximal holes on local wall shear stress distribution. (a) and (b) are wall shear stress heat-maps without blockage. (c) and (d) show that a partial blockage results in the formation of zones with lower wall shear stress (4 mPa), compared with that of the unblocked case (15 mPa), which corresponds to schematics (a) and (b). The catheter used here is that from the Scenario 1 in §4.2. Both cases were simulated with the same total flow rate of 0.3 mL/min.